

Characterizing Extreme Emission-line Galaxies. I. A Four-zone Ionization Model for Very High-ionization Emission*

Danielle A. Berg 1, John Chisholm 1, Dawn K. Erb 2, Evan D. Skillman 3, Richard W. Pogge 4, 0, and Grace M. Olivier 4, Evan D. Skillman 3, Richard W. Pogge 4, 0, and Grace M. Olivier 4, Evan D. Skillman 3, Richard W. Pogge 4, 5, and Grace M. Olivier 4, Evan D. Skillman 3, Richard W. Pogge 4, 5, and Grace M. Olivier 4, Evan D. Skillman 3, Evan D. Skillman 3, Evan D. Skillman 3, Evan D. Skillman 3, Evan D. Skillman 4, Evan D Department of Astronomy, The University of Texas at Austin, 2515 Speedway, Stop C1400, Austin, TX 78712, USA; daberg@austin.utexas.edu ² Center for Gravitation, Cosmology, and Astrophysics, Department of Physics, University of Wisconsin Milwaukee, 3135 N Maryland Avenue, Milwaukee, WI 53211, USA

³ Minnesota Institute for Astrophysics, University of Minnesota, 116 Church Street SE, Minneapolis, MN 55455, USA Department of Astronomy, The Ohio State University, 140 W 18th Avenue, Columbus, OH 43210, USA ⁵ Center for Cosmology & AstroParticle Physics, The Ohio State University, 191 W Woodruff Avenue, Columbus, OH 43210, USA Received 2021 April 3; revised 2021 July 12; accepted 2021 July 12; published 2021 November 29

Abstract

Stellar population models produce radiation fields that ionize oxygen up to O⁺², defining the limit of standard H II region models (<54.9 eV). Yet, some extreme emission-line galaxies, or EELGs, have surprisingly strong emission originating from much higher ionization potentials. We present UV HST/COS and optical LBT/MODS spectra of two nearby EELGs that have very high-ionization emission lines (e.g., He II $\lambda\lambda$ 1640,4686 C IV $\lambda\lambda$ 1548,1550, [Fe V] λ 4227, [Ar IV] $\lambda\lambda$ 4711,4740). We define a four-zone ionization model that is augmented by a very highionization zone, as characterized by He⁺² (>54.4 eV). The four-zone model has little to no effect on the measured total nebular abundances, but does change the interpretation of other EELG properties: we measure steeper central ionization gradients; higher volume-averaged ionization parameters; and higher central T_e , n_e , and log U values. Traditional three-zone estimates of the ionization parameter can underestimate the average $\log U$ by up to 0.5 dex. Additionally, we find a model-independent dichotomy in the abundance patterns, where the α/H abundances are consistent but N/H, C/H, and Fe/H are relatively deficient, suggesting these EELGs are α /Fe-enriched by more than three times. However, there still is a high-energy ionizing photon production problem (HEIP³). Even for such α /Fe enrichment and very high log Us, photoionization models cannot reproduce the very high-ionization emission lines observed in EELGs.

Unified Astronomy Thesaurus concepts: Dwarf galaxies (416); Ultraviolet astronomy (1736); Galaxy chemical evolution (580); Galaxy spectroscopy (2171); High-redshift galaxies (734); Emission line galaxies (459)

1. Introduction

1.1. Background

The 21st century of astronomy has been marked by deep imaging surveys with the Hubble Space Telescope (HST) that have opened new windows onto the high-redshift universe, unveiling thousands of z > 6 galaxies (e.g., Bouwens et al. 2015; Finkelstein et al. 2015; Livermore et al. 2017; Atek et al. 2018; Oesch et al. 2018). From these studies, and the numerous sources discovered, a general consensus has emerged that lowmass galaxies host a substantial fraction of the star formation in the high-redshift universe and are likely the key contributors to reionization (e.g., Wise et al. 2014; Madau & Haardt 2015; Robertson et al. 2015; Stanway et al. 2016).

Significant observational efforts have been invested in the study of these reionization era systems, revealing a population of compact, metal-poor, low-mass sources with blue UV continuum slopes that are rare at $z \sim 0$ (e.g., Laporte et al. 2017; Mainali et al. 2017; Stark et al. 2017; Hutchison et al. 2019). Deep rest-frame UV spectra of z > 5 galaxies have revealed prominent high-ionization nebular emission lines (i.e., O III], C III], C IV, He II), with especially large C III] and C IV equivalent widths (\sim 20–40 Å), indicating that extreme radiation fields characterize reionization-era galaxies (Sobral et al. 2015; Stark et al. 2015; Stark 2016; Mainali et al. 2017, 2018). Further, in the spectral energy distributions of z > 6 galaxies, Spitzer/IRAC 3.6–4.5 μ photometry has revealed strong, excess emission attributed to nebular H β +[O III] $\lambda\lambda$ 4959,5007 emission (rest-frame EW(H β +[O III]) \sim 600–800 Å; e.g., Labbé et al. 2013; Smit et al. 2015; De Barros et al. 2019; Endsley et al. 2021). These large optical and UV nebular emission equivalent widths (EWs) require small continuum fluxes relative to the emission lines, which can result from large bursts of star formation. Despite these considerable advances in characterizing reionization era galaxies, the spatial and spectral limitations of observing faint, distant galaxies have left the physical processes regulating this dynamic evolutionary phase poorly constrained.

1.2. Extreme Emission-line Galaxies

In order to characterize the most distant galaxies that the next generation of telescopes will observe, an expanded framework of local galaxies encompassing more extreme properties is needed. In particular, it is important to understand the conditions that produce similarly large emission-line EWs in star-forming galaxies as seen at high redshifts, so-called extreme emission-line galaxies (EELGs). In the past few years, progress has been made by observational campaigns focused on EELGs at lower redshifts with very large optical emissionline EWs. At $z \sim 0-2$, studies of large samples of galaxies with large $[OIII]+H\beta$ EWs find that the extreme nebular emission is associated with a recent burst of star formation in low-mass galaxies that results in highly ionized gas (e.g., Atek et al. 2011; van der Wel et al. 2011; Maseda et al. 2013, 2014; Chevallard et al. 2018; Tang et al. 2019).

^{*} Based on observations made with the NASA/ESA Hubble Space Telescope, obtained from the Data Archive at the Space Telescope Science Institute, which is operated by the Association of Universities for Research in Astronomy, Inc., under NASA contract NAS 5-26555.

Other studies have focused on EELGs with large EWs of UV emission lines. For instance, some studies of lensed galaxies at $z\sim 2-3$ measure strong nebular C IV $\lambda\lambda 1548,1550$ and He II $\lambda 1640$ emission (e.g., Christensen et al. 2012; Stark et al. 2014; Vanzella et al. 2016, 2017; Schmidt et al. 2017; Smit et al. 2017; Berg et al. 2018; McGreer et al. 2018), while studies of nearby dwarf galaxies have empirically demonstrated that strong C IV $\lambda\lambda 1547,1550$, He II $\lambda 1640$, and C III] $\lambda\lambda 1907,1909$ emission requires low metallicities (Z < 0.1 Z $_{\odot}$) and young, large bursts of star formation (as indicated by large [O III] $\lambda 5007$ EWs; e.g., Rigby et al. 2015; Berg et al. 2016; Senchyna et al. 2017, 2019; Berg et al. 2019a, 2019b; Tang et al. 2021.)

However, even among these EELG studies, it is difficult to find galaxies with UV emission comparable to that seen in reionization era systems. Recently, Tang et al. (2021) observed the rest-frame UV emission lines in a sample of 1.3 < z < 3.7 galaxies with high specific star formation rates (sSFRs), finding that only metal-poor emitters with intense ${\rm H}\beta+[{\rm O\,III}]~\lambda5007$ EWs >1500 Å had C III] emission strengths comparable to those seen at z>6. While previous UV studies of local, metal-poor galaxies have reported a handful of C III] $\lambda\lambda1907,1909$ EWs >15 Å, these observations lacked the coverage and resolution necessary for detailed nebular studies (e.g., Berg et al. 2016: J082555, J104457; Berg et al. 2019b: J223831, J141851, J121402, J171236, J095430, J094718). Here, we study high-quality UV and optical spectra of two nearby EELGs with the largest reported C III] $\lambda\lambda1907,1909$ EWs at $z\sim0$ to date.

1.3. Two Nearby EELGs: J104457 and J141851

J104457 ($10^h44^m57^s.790 + 03^\circ53'13''.10$) and J141851 ($14^h18^m51^s.119 + 21^\circ02'39''.84$]) were originally selected for UV spectroscopic study based on their properties as derived from their optical Sloan Digital Sky Survey observations. Specifically, J104457 and J141851 are nearby, compact, low-stellar-mass, metal-poor, UV-bright galaxies with high specific star formation rates and significant high-ionization emission (EW [O III] $\lambda5007 > 1000$ Å; see Table 1). These properties place J104457 and J141851 in the class of blue compact dwarf (BCD) galaxies with intense starburst episodes on spatial scales of $\lesssim 1$ kpc (see, e.g., Papaderos et al. 2008). We use the detailed observations of these metal-poor galaxies as unique laboratories to investigate the nebular and stellar properties in nearly pristine conditions that are analogous to the early universe.

Here we present part I of a detailed analysis of the UV HST/COS G160M and optical LBT/MODS spectra of J104457 and J141851, focused on the emission lines and nebular properties. Part II will expand on this analysis by simultaneously modeling the ionizing stellar population and will be presented in G. Olivier et al. (2021, in preparation).

This paper is organized as follows. We describe the UV and optical spectroscopic observations in Section 2. In Section 3.1, we introduce a four-zone nebular ionization model and calculate the subsequent physical properties: direct temperature and density measurements are presented in Section 3.2.1, followed by a discussion of their structure, while the ionization structure is analyzed in Section 3.2.2. We then determine nebular abundances, presenting O/H in Section 4.1, new ionization correction factors in Section 4.2, N/O in Section 4.3, C/O in Section 4.4, α -elements/O in Section 4.5, and Fe/O in Section 4.6. We discuss the physical properties of EELGs in Section 5, where we focus on the resulting differences from using a three-zone versus four-zone ionization model in interpreting individual abundances in

 Table 1

 Extreme Emission-line Galaxy Properties

Property	J104457	J141851
Adopted	from Archival Sources:	
Reference	Berg+16	Berg+19a
R.A. (J2000)	10:44:57.79	14:18:51.13
Decl. (J2000)	+03:53:13.15	+21:02:39.74
z	0.013	0.009
$\log M_{\star} (M_{\odot})$	6.80	6.63
$\log SFR (M_{\odot} yr^{-1})$	-0.85	-1.16
log sSFR (yr ⁻¹)	-7.64	-7.79
E(B-V) (mag)	0.077	0.140
$12 + \log(O/H) (dex (Z_{\odot}))$	7.45 (0.058)	7.54 (0.071)
$\log U$	-1.77	-2.42
Derived from t	the UV COS G160M Spec	etra:
$\mathrm{EW}_{\mathrm{O\ III}}(\mathring{\mathrm{A}})$	-2.89, -6.17	-1.68, -4.78
EW _{C IV} (Å)	-6.71, -2.83	-1.78, -1.43
EW _{He II} (Å)	-2.75	-2.82
EW _{C III]} (Å)	-16.35	-18.41

Note. Properties of the extreme emission-line galaxies presented here. The top portion of the table lists properties previously reported by Berg et al. (2016) for J104457 and Berg et al. (2019b) for J141851. The R.A., decl., redshift, total stellar masses, SFRs, and sSFRs were adopted from the SDSS MPA-JHU DR8 catalog^a, whereas E(B-V), $12 + \log(O/H)$, and $\log U$, were measured from the SDSS optical spectra. The bottom portion of the table lists the properties derived from the UV HST/COS G160M spectra. Equivalent widths are listed for C IV $\lambda\lambda$ 1548,1550, O III] $\lambda\lambda$ 1661,66, He II λ 1640, and C III] $\lambda\lambda$ 1907,09.

^a Data catalogs are available from http://www.sdss3.org/dr10/spectro/galaxy_mpajhu.php. The Max Plank institute for Astrophysics/John Hopkins University(MPA/JHU) SDSS database was produced by a collaboration of researchers (currently or formerly) from the MPA and the JHU. The team is made up of Stephane Charlot (IAP), Guinevere Kauffmann and Simon White (MPA), Tim Heckman (JHU), Christy Tremonti (U. Wisconsin-Madison – formerly JHU) and Jarle Brinchmann (Leiden University – formerly MPA).

Section 5.1. We introduce the high-energy ionizing photon production problem in Section 5.2 and then consider the overall abundance and ionization profiles of EELGs in Section 5.3 and Section 5.4, respectively. Finally, we make recommendations for interpreting the spectra of EELGs in Section 5.5 and summarize our findings in Section 6.6

2. High S/N Spectral Observations

2.1. HST/COS FUV Spectra

The high-resolution HST/COS G160M spectra for J104457 and J141851 were first presented in Berg et al. (2019a) to discuss their abnormally strong C IV and He II emission. We briefly summarize the observations here. The HST/COS observations were observed by program HST-GO-15465 (PI:

⁶ A note about notation: we adopt standard ion and spectroscopic notation to describe the ionization states that give rise to different emission lines. In this manner, a given element, X, with i ionizations is denoted as an X^{+i} ion that can produce an emission line via radiative decay given by X followed by the Roman numeral i+1 or via recombination given by X followed by the Roman numeral i. For example, the numeral I is used to represent neutral elements, II to represent the first ionization state, III to represent the second ionization state, and so on. Additionally, square brackets are used to denote forbidden transitions, whereas semi-forbidden transitions use only the closing bracket and allowed transitions do not use brackets at all. For example, recombination of the He⁺² ion produces allowed He II emission and radiative decay of the collisionally excited O^{+2} ion produces forbidden [O III] emission. We will use this ion and spectroscopic notation interchangeably throughout this work.

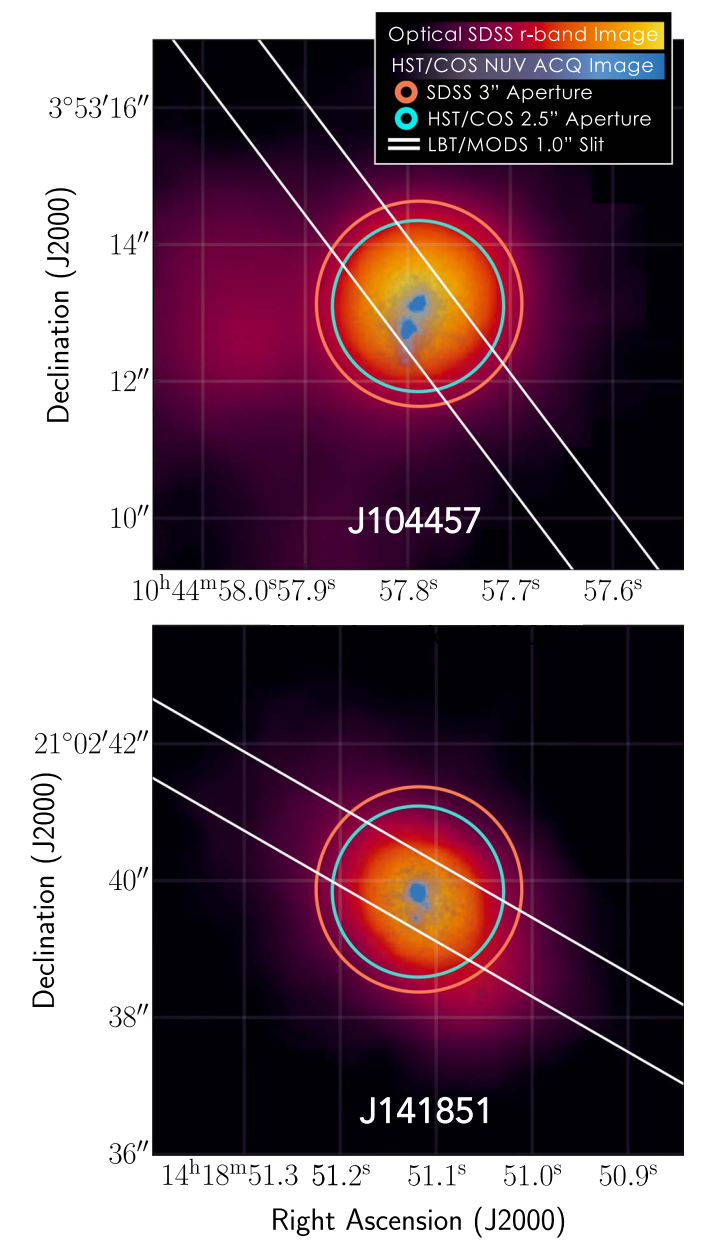


Figure 1. HST/COS NUV acquisition images of J104457 (top) and J141851 (bottom) are shown in blue, overlaid on top of the SDSS *r*-band image (red to yellow color bar). The 2".5 COS aperture used for the UV spectra is shown as a blue circle and is very similar to the SDSS 3" aperture in orange. In comparison, the 1" LBT/MODS slit (white lines) captures most of the NUV light but may miss a significant fraction of the extended nebular emission. Note that J104457 has a fainter companion to the east (left) visible in the optical, but this was not captured in the optical or UV spectra used here.

Berg). Utilizing the coordinates obtained through previous low-resolution COS G140L observations of these two targets, target acquisitions were efficiently achieved using the IM/ACQ mode with the PSA aperture and Mirror A. The NUV acquisition images of J104457 and J141851 are shown in Figure 1, demonstrating that they are high-surface-brightness, star-forming galaxies being dominated by just a few stellar clusters.

The COS FUV science observations were taken in the TIME-TAG mode using the 2".5 PSA aperture and the G160M grating at a central wavelength of 1589 Å, for total exposures of 6439 and 12374 s for J104457 and J141851, respectively.

We used the FP-POS = ALL setting, which takes four images offset from one another in the dispersion direction, increasing the cumulative S/N and mitigating the effects of fixed pattern noise. Spectra were processed with CALCOS version 3.3.4.

In order to improve the signal-to-noise, we binned the spectra by 6 native COS pixels such that $\Delta \nu = 13.1 \, \mathrm{km \, s^{-1}}$, but the emission-line FWHMs are still sampled by more than 4 pixels. The resulting FUV spectra, shown in Figure 2, have wavelength coverage that is rich in nebular features not found in the optical.

2.2. LBT/MODS Optical Spectra

We obtained optical spectra of J104457 and J141851 using the Multi-Object Double Spectrographs (MODS, Pogge et al. 2010) on the Large Binocular Telescope (LBT, Hill et al. 2010) on the UT dates of 2018 May 19 and 18, respectively. The conditions were clear, with good seeing (\sim 0."7 for J104457 and \sim 0."8 for J141851) and low variability (<0."1 over the total science integrations). MODS is a moderate-resolution $(R \sim 2000)$ optical spectrograph with large wavelength coverage $(3200 \le \lambda \le 10,000 \text{ Å})$. Simultaneous blue and red spectra were obtained using the G400L (400 lines mm⁻¹, $R \approx 1850$) and G670L (250 lines mm⁻¹, $R \approx 2300$) gratings, respectively. J104457 and J141851 were observed using the $1'' \times 60''$ long slit for 3×900 s exposures, or 45 min of total exposure per object. The slits were centered on the highest surface brightness knot of optical emission as determined from the Sloan Digital Sky Survey (SDSS) r-band image and oriented to the parallactic angle at half the total integration time. Both targets were observed at air masses of less than 1.2, which served to minimize flux losses to differential atmospheric refraction (Filippenko 1982). The slit orientations of the MODS observations are shown relative to the HST/COS NUV acquisition images in Figure 1, demonstrating that the peak of the optical and UV surface brightness profiles are aligned and that most of the stellar light is captured within the slit. However, in comparison to the extended nebular emission that is contained within the 2."5 COS aperture, the MODS observations may suffer from significant losses of extended emission.

Spectra were reduced, extracted, and analyzed using the beta version of the MODS reduction pipeline⁸ which runs within the XIDL⁹ reduction package. One-dimensional spectra were corrected for atmospheric extinction and flux-calibrated based on observations of flux standard stars (Oke 1990). The details of the MODS reduction pipeline are further described by Berg et al. (2015); while that work analyzes multi-object multiplexed spectra, the major steps are identical to that of the present long-slit reduction. The resulting optical spectra are shown in Figure 3.

2.3. Emission-line Measurements

For this work, we measured all of the emission-line fluxes in a consistent manner when possible. For the optical LBT/MODS spectra, we used the continuum-modeling and line-fitting code developed as part of the CHAOS project (Berg et al. 2015). First, the underlying continuum of the optical spectra were fit by the

https://www.stsci.edu/hst/instrumentation/cos/documentation/calcos-

⁸ http://www.astronomy.ohio-state.edu/MODS/Software/modsIDL/

http://www.ucolick.org/~xavier/IDL/

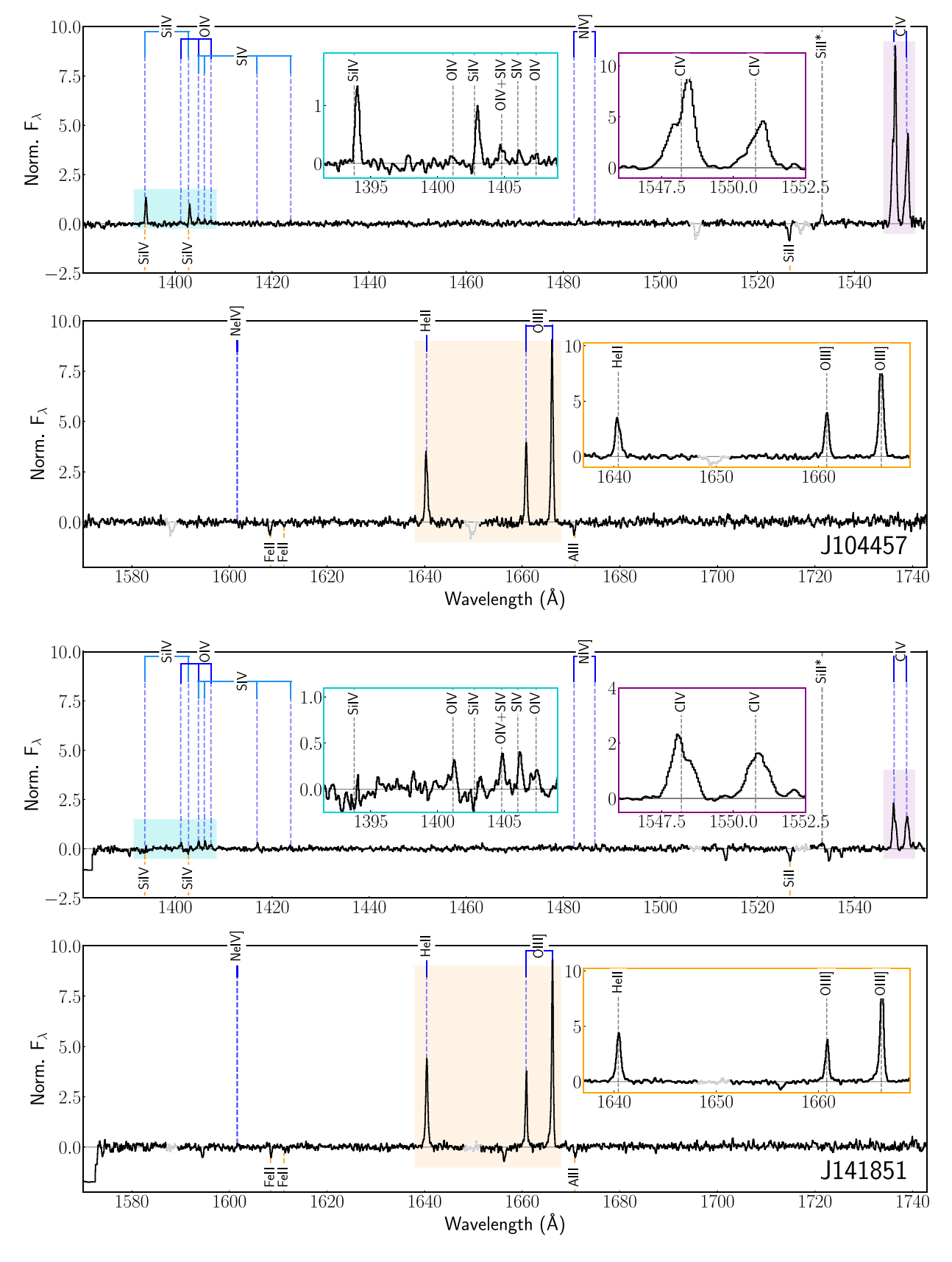


Figure 2. High-resolution HST/COS G160M UV spectra of J104457 (top two panels) and J141851 (bottom two panels). Emission features are labeled at the top of each spectrum, whereas potential ISM absorption features are labeled below and Milky Way lines are plotted in gray the strong, high-ionization emission lines that are characteristic of EELGs and are highlighted in the purple and orange inset windows (i.e., C IV, He II, and O III]). Plotting the full G160M spectra reveals additional high-ionization emission lines from Si IV, O IV, and S IV as seen in the blue inset window. These rare, extreme high-ionization emission lines support the hypothesis that these targets are similar to reionization-era systems, producing copious amounts of very high-energy ionizing photons.

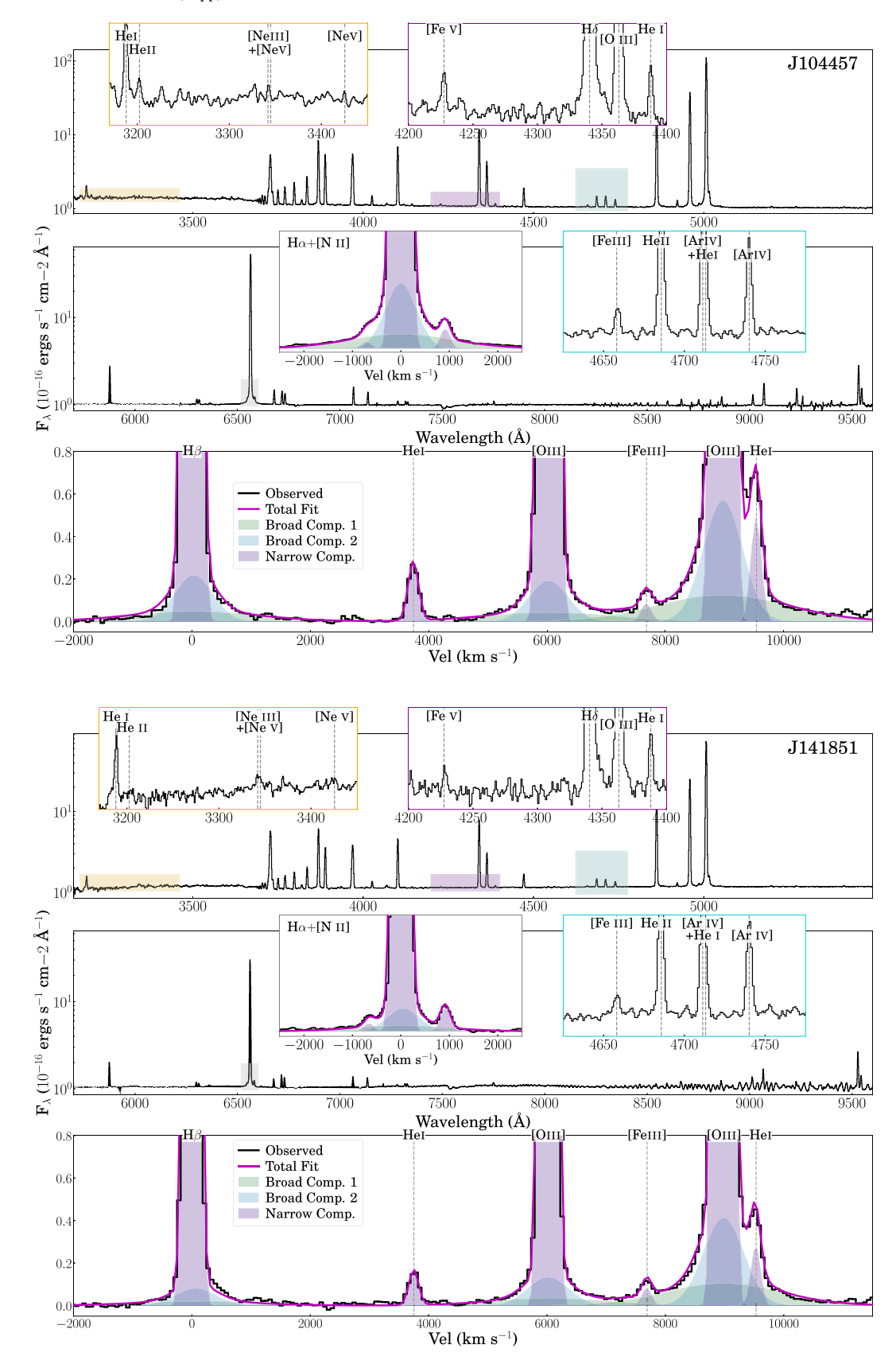


Figure 3. Optical MODS/LBT spectra of J104457 (top three panels) and J141851 (bottom three panels). With expansive wavelength coverage from roughly 3200–10,000 Å, these spectra feature numerous T_e and n_e diagnostic emission lines that span a wide range of ionization zones. Additionally, the colored inset windows highlight emission from very high-ionization species: the yellow and blue windows highlight the rare [Ne III] $\lambda 3342$ T_e -sensitive and [Ar IV] $\lambda \lambda 4711,4740$ n_e -sensitive features that can be used to characterize the properties of the very high-ionization zone, while the purple inset window highlights the narrow, rare [Fe V] emission. For the strongest emission lines, we also see weak broad emission. The gray inset windows reveal broad emission at the base of the Hα emission, suggesting an additional source of energy such as from shocks. The bottom panels show fits that are scaled from the multi-component Hα fits.

STARLIGHT¹⁰ spectral synthesis code (Fernandes et al. 2005) using stellar models from Bruzual & Charlot (2003). Next, emission lines were fit in the continuum-subtracted spectrum with Gaussian profiles and allowing for an additional nebular continuum component. The fit parameters (i.e., width, line center) of neighboring lines were constrained, allowing weak or blended features to be measured simultaneously. For both J104457 and J141581, we measure Gaussian full-width at half-maximum (GFWHM) values of roughly 3.5 and 5.5 Å in the blue and red spectra, respectively. With a linear spectral dispersion of 0.5 and 0.8 Å pix⁻¹ for the red and blue, respectively, our narrow lines are well sampled. However, our GFWHMs correspond to $\Delta v_{\rm blue} \approx 200 \, {\rm km \, s^{-1}}$ at $\lambda 5007$ and $\Delta v_{\rm red} \approx 250 \, {\rm km \, s^{-1}}$ at $\lambda 6563$, and, as a result, these spectra are not sensitive to broad components of comparable velocity width

Broad components can occur in the presence of stellar winds or shocks. In the case of the He II $\lambda 1640$ and $\lambda 4686$ lines, we allow for additional broad components but do not find evidence for any; with velocity widths consistent with the other emission lines, this suggests that the He II emission is nebular in origin. However, for the strongest optical emission lines (H β , [O III] $\lambda\lambda 4959,5007$, and H α), we measure multi-component fits, as shown in Figure 3. These lines all have (1) strong, narrow nebular components, (2) moderate, broad components, and (3) weak, very broad components with similar velocity profiles, but where the scaled broad components of the H α and H β features are stronger relative to those of the [O III] emission lines. This could suggest that the broad emission is more strongly produced in the low-ionization gas than the high-ionization gas. Another possible explanation is that the broad emission is coming from higher-density regions that suppress forbidden emission.

Interestingly, the two broad components of both galaxies have large velocity widths of roughly 2500 and 750 km s⁻¹. These are especially large velocities compared to the small circular velocities of these galaxies ($v_{circ} = 16.6$ and $12.1 \,\mathrm{km \, s^{-1}}$ for J104457 and J141851, respectively, derived using the equation from Reyes et al. 2011) and the lack of outflows measured from the UV absorption line spectra (see Figure 3 in Berg et al. 2019a). However, each broad component only accounts for 1%-3% of the total $H\alpha$ flux. Broad component emission for H β , [O III], and H α are often seen in the spectra of blue compact dwarf galaxies (BCDs; e.g., Izotov et al. 2006; Izotov & Thuan 2007) with similar widths $(1000-2000 \,\mathrm{km \, s^{-1}})$ and fractional fluxes of 1%-2%. While broad emission represents a small fraction of the H β and H α fluxes, it can significantly affect the fit to the weak [NII] $\lambda\lambda6548,6584$ lines. For this reason we adopt the narrow-line fluxes from our multi-component fits for our analysis, but do not investigate the the broad emission further.

For the UV HST/COS spectra, no continuum model was used. Similar to the optical lines, we measured the nebular emission-line strengths using constrained Gaussian profiles. In addition to the C IV, He II, O III], Si III], and C III] features that were previously detected in the low-resolution G140L spectra, we identify and measure emission from Si IV, O IV, S IV, and Si II* features in the G160M spectra (see Figure 2).

Flux measurements for both the UV and optical lines were corrected for Galactic extinction using the PYTHON DUSTMAPS interface (Green 2018) to query the Green et al. (2015)

 ${\bf Table~2} \\ {\bf UV+Optical~Emission~Lines~from~HST/COS~and~LBT/MODS~Observations}$

UV+Optical Emission Lin	es from HS1/COS and LB1,	/MODS Observations
Ion+Wavelength	J104457	J141851
	UV Lines: $I(\lambda)/IO$ III]	
Si IV λ1393.76	10.4 ± 2.5	
O IV λ1401.16	2.2 ± 2.2	3.6 ± 3.0
Si IV λ1402.77	6.7 ± 2.4	•••
O IV+SIV λ 1404.81	3.5 ± 2.4	4.9 ± 3.0
S IV $\lambda 1406.02$	2.9 ± 2.4	3.3 ± 3.0
O IV λ1407.38	0.7 ± 2.4	1.6 ± 3.0
S IV λ1416.89	<2.7	1.8 ± 3.0
S IV λ1423.85	<3.3	2.1 ± 3.0
N IV] λ1483.33 N IV] λ1486.50	2.7 ± 3.3 1.3 ± 3.3	2.0 ± 3.0 1.6 ± 3.0
SiII* λ1533.43	6.8 ± 3.9	6.0 ± 3.8
C IV λ1548.19	149.0 ± 9.6	39.5 ± 4.3
C IV λ1550.77	71.7 ± 5.8	30.5 ± 4.1
He II $\lambda 1640.42$	42.8 ± 6.3	58.8 ± 5.8
O III] λ1660.81	45.7 ± 6.4	40.2 ± 5.3
O III] λ1666.15	100.0 ± 8.2	100.0 ± 7.1
Si III] λ1883.00	43.9 ± 14.3	42.0 ± 13.1
Si III] λ1892.03	36.7 ± 2.8	29.9 ± 13.0
C III] λ1906.68	135.8 ± 18.4	162.2 ± 9.7
[C III] λ1908.73	106.7 ± 17.7	110.0 ± 6.6
E(B-V) _{R16}	0.086 ± 0.042	0.036 ± 0.050
F _{O III]}	523.9 ± 30.5	275.7 ± 13.8
(Optical Lines: $I(\lambda)/I(H\beta)$	
He Iλ3188.75	2.86 ± 0.11	3.85 ± 0.17
He II $\lambda 3203.00$	0.60 ± 0.10	0.47 ± 0.16
[Ne III] $\lambda 3342.18$	0.33 ± 0.10	0.59 ± 0.16
[Ne V] $\lambda 3345.82$	< 0.06	0.64 ± 0.16
[Ne V] $\lambda 3425.88$	0.11 ± 0.10	0.60 ± 0.16
[O II] λ3726.04	9.60 ± 0.15	14.43 ± 0.27
[O II] λ3728.80	16.77 ± 0.23	34.91 ± 0.43
He I $\lambda 3819.61$	0.92 ± 0.02	1.12 ± 0.03
H9 λ3835.39	7.19 ± 0.10	7.24 ± 0.11
[Ne III] $\lambda 3868.76$	31.73 ± 0.45	37.64 ± 0.51 1.96 ± 0.04
He I λ3888.65		
H8 λ3889.06	0.82 ± 0.13	17.10 ± 0.20
He I λ3964.73	6.89 ± 0.10	3.15 ± 0.08
[Ne III] $\lambda 3967.47$	13.41 ± 0.18	10.62 ± 0.17
H7 λ3970.08	5.47 ± 0.20	13.80 ± 0.21
He I $\lambda 4026.19$ [S II] $\lambda 4068.60$	1.72 ± 0.03 0.38 ± 0.01	1.86 ± 0.04 0.71 ± 0.05
[S II] λ4076.35	0.38 ± 0.01 0.15 ± 0.01	0.71 ± 0.03 0.28 ± 0.03
Hδ λ 4101.71	25.59 ± 0.42	25.76 ± 0.39
He I λ 4120.81	0.26 ± 0.02	0.30 ± 0.02
He I $\lambda 4143.15$	0.25 ± 0.09	0.30 ± 0.16
[Fe V] $\lambda 4227.19$	0.03 ± 0.01	0.15 ± 0.02
H $\gamma \lambda 4340.44$	46.55 ± 0.67	47.31 ± 0.68
[O III] λ4363.21	13.51 ± 0.21	13.80 ± 0.23
He I λ4387.93	0.47 ± 0.01	0.49 ± 0.01
He I λ4471.48	3.97 ± 0.09	7.08 ± 0.16
[Fe III] $\lambda 4658.50$	0.34 ± 0.03	0.43 ± 0.02
He II λ4685.70	1.80 ± 0.04	2.15 ± 0.03
[Ar IV] $\lambda 4711.37^{a}$	1.65 ± 0.06	3.21 ± 0.08
He I $\lambda 4713.14^{b}$	0.32 ± 0.01	0.57 ± 0.02
[Ar IV] $\lambda 4740.16$	1.16 ± 0.02	2.51 ± 0.06
Hβ λ4861.35 ^c	100.0 ± 1.4	100.0 ± 1.4
[Fe IV] $\lambda 4906.56$	0.08 ± 0.06	< 0.03
He I $\lambda 4921.93$	1.05 ± 0.19	0.99 ± 0.29
[O III] $\lambda 4958.91^{\circ}$	143.0 ± 1.5	162.5 ± 1.7
[Fe III] $\lambda 4985.87^{\circ}$	0.04 ± 0.09	0.85 ± 0.15
[O III] $\lambda 5006.84^{\circ}$	427.5 ± 4.3	500.7 ± 5.0
He I $\lambda 5015.68^{c}$	1.82 ± 0.05	1.65 ± 0.12

¹⁰ www.starlight.ufsc.br

Table 2 (Continued)

	(Continued)	
Ion+Wavelength	J104457	J141851
[Fe II] λ5158.79	0.08 ± 0.09	< 0.03
[Fe III] $\lambda 5270.40$	0.15 ± 0.09	< 0.03
[N II] λ5754.59	< 0.09	< 0.33
He I $\lambda 5875.62$	10.17 ± 0.15	9.96 ± 0.18
[O I] $\lambda 6300.30$	0.86 ± 0.05	1.50 ± 0.08
[S III] $\lambda 6312.06$	0.80 ± 0.03	1.21 ± 0.11
[O I] $\lambda 6363.78$	0.25 ± 0.03	0.66 ± 0.05
[N II] $\lambda 6548.05^{\circ}$	0.27 ± 0.05	0.56 ± 0.05
$H\alpha \lambda 6562.79^{c}$	296.7 ± 4.2	275.8 ± 3.9
[N II] $\lambda 6583.45^{\circ}$	0.81 ± 0.05	1.68 ± 0.05
He I $\lambda 6678.15$	2.85 ± 0.05	2.63 ± 0.06
[S II] $\lambda 6716.44$	2.50 ± 0.04	4.04 ± 0.13
[S II] $\lambda 6730.82$	2.04 ± 0.05	2.99 ± 0.06
He I $\lambda 7065.19$	3.57 ± 0.05	3.36 ± 0.07
[Ar III] $\lambda 7135.80$	2.42 ± 0.09	2.98 ± 0.11
[O II] λ7319.92	0.60 ± 0.02	0.80 ± 0.05
[O II] λ7330.19	0.48 ± 0.07	0.71 ± 0.06
[Ar III] λ 7751.06	0.45 ± 0.03	1.03 ± 0.05
P13 λ8665.02	1.05 ± 0.03	2.18 ± 0.07
P12 λ8750.46	0.93 ± 0.05	0.78 ± 0.05
P11 λ8862.89	1.44 ± 0.07	2.34 ± 0.07
P10 λ9015.30	1.80 ± 0.05	3.46 ± 0.10
[S III] $\lambda 9068.60$	4.24 ± 0.07	6.18 ± 0.10
P9 λ9229.70	3.06 ± 0.06	1.58 ± 0.09
[S III] $\lambda 9530.60$	10.10 ± 0.14	15.39 ± 0.23
E(B-V)	0.039 ± 0.017	0.019 ± 0.016
$F_{H\beta}$	95.2 ± 1.0	55.7 ± 0.6

Notes. Reddening-corrected emission-line intensities from the high-resolution UV HST/COS G160M spectra and optical LBT/MODS spectra for J104457 and J141851. The Si III] and C III] lines (italicized) are exceptions and are from the low-resolution HST/COS G140L spectra. Fluxes for undetected lines are given as less than their 3σ upper limits. The UV fluxes have been modified to a common scale and are given relative to the (O III] λ 1666 flux, multiplied by 100, from the G160M spectra. The optical fluxes are given relative to H β ×100. The last two rows below the UV lines list the dust extinction derived using the Reddy et al. (2016) reddening law and the raw, observed fluxes for O III] λ 1666, in units of 10^{-16} erg s⁻¹ cm⁻². The last two rows below the optical lines list the dust extinction using the Cardelli et al. (1989) reddening law and the raw, observed fluxes for H β , in units of 10^{-16} erg s⁻¹ cm⁻². Details of the spectral reduction and line measurements are given in Section 2.

extinction map, with a Cardelli et al. (1989) reddening law. Then, the relative intensities of the four strongest Balmer lines $(\text{H}\alpha/\text{H}\beta,\,\text{H}\gamma/\text{H}\beta,\,\text{H}\delta//\text{H}\beta)$ were used to determine the dust-reddening values, E(B-V), for both the Cardelli et al. (1989) and Reddy et al. (2016) laws. Finally, these E(B-V) values were used to reddening-correct the other emission lines, assuming a Cardelli et al. (1989) extinction law in the optical and a Reddy et al. (2016) law in the UV. The uncertainty measured for each line is a combination of the spectral variance, flux-calibration uncertainty, Poisson noise, read noise, sky noise, flat-fielding uncertainty, and uncertainty in the reddening determination.

We note that the significant detections of the O III] $\lambda 1661,1666$ emission doublet in both the G140L and G160M allowed us to place our relative emission-line measurements on a common scale. We, therefore, scaled the Si III] and C III] emission-line fluxes from the low-resolution G140L spectra by the O III] $I_{\lambda 1666,G160M}/I_{\lambda 1666,G140L}$ flux ratio and included them in our subsequent analysis of the G160M emission lines. The reddening-corrected, scaled emission-line intensities measured for the UV HST/COS and optical LBT/MODS spectra of J104457 and J141851 are reported in Table 2, respectively.

2.4. The Effect of Aperture on Relative Flux

In order to utilize our high-S/N HST/COS UV spectra and *LBT*/MODS optical spectra together, we must consider the effect of aperture losses in the 1" MODS long slit versus the COS 2."5 aperture. Such a comparison can be done using the *LBT*/MODS optical spectra for J104457 and J141851 and their corresponding SDSS optical spectra, which were observed with an aperture (3") that is similar to that of COS. To do so, we normalized each spectrum by its average continuum flux in the relatively featureless wavelength regime of 4500–4600 Å in order to compare the relative line strengths of interest. We find that the percent differences in emission-line fluxes are typically <5%, suggesting that an aperture correction is not required. Further, these differences are not systematic, precluding an accurate aperture correction unless the exact 2D ionization structure can be determined.

Interestingly, the differences between low-ionization and high-ionization species are similarly small for J104457, however, the differences are larger for the low-ionization species than the high-ionization species in the J141851 spectra. This situation would naturally result from the aperture differences given a simple H II region structure with the high-ionization region concentrated in the center and the low-ionization region being more extended. Additionally, we compared the same temperature and density measurements we describe in Section 3.2.1 for the LBT/MODS spectra and SDSS spectra, but find that the results agree within the uncertainties. We, therefore, do not apply any aperture corrections to the MODS optical spectra and do not find any strong evidence that this will affect comparisons between the UV and optical data. However, it is important to note that this result is only true for the relative flux comparisons; the absolute flux correction of SDSS/MODS is roughly a factor of 51 for J104457 and 47 for J141851.

3. Improved Nebular Properties: Harnessing the UV +Optical

3.1. An Updated Ionization Model of EELGs

Previous nebular abundance determinations for J104457 and J141851 were reported in Berg et al. (2016) and Berg et al. (2019b), respectively. Those works followed the standard best-practice methodology of determining total and relative abundances using the *direct method* (i.e., measuring the electron temperature and density) and assuming a classic three-zone ionization model. In the top of Figure 4 we plot the ionization potential energies of several important interstellar medium (ISM) ions relative to the three-zone ionization model, where the ionization potential energy ranges of N^+ , S^{+2} , and O^{+2} define the low-, intermediate-, and high-ionization zones,

^a At the spectral resolution of the LBT/MODS spectra, we observe [Ar IV] λ 4711+He I λ 4713 as a blended line profile. Therefore, the predicted He I λ 4713 flux is subtracted to determine the residual [Ar IV] λ 4711 flux.

^b The He I λ 4713 flux was predicted from the observed He I λ 4471 flux and their relative emissivities, as determined by PYNEB.

^c These line fluxes were corrected for the additional broad emission components seen in Figure 3. Only the narrow components are listed here.

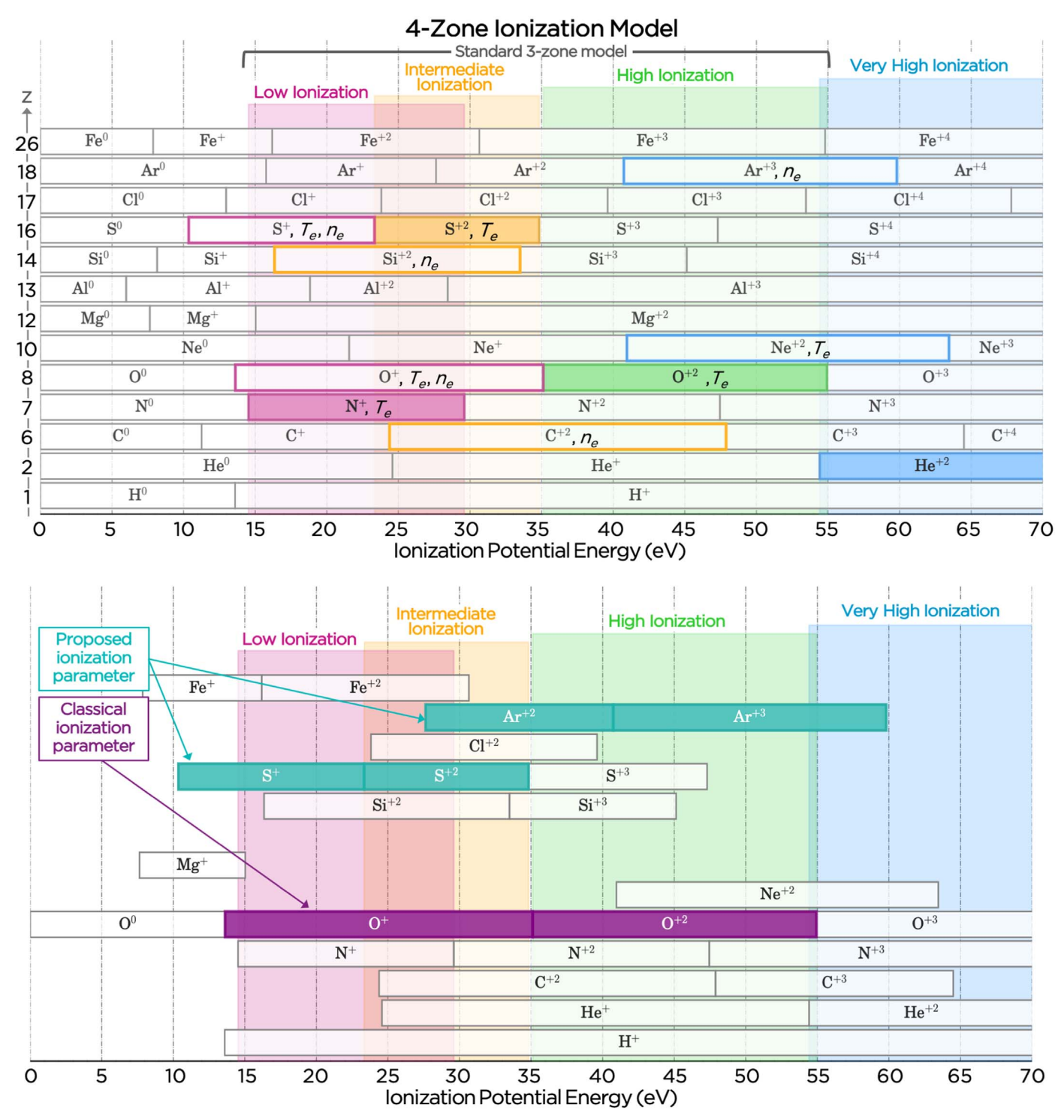


Figure 4. Top: ionization potential energies (eV) of important ISM species, ordered vertically by their atomic numbers (Z). The figure is divided horizontally into different gas ionization zones, where the classical three-zone model for star-forming regions defines low-ionization by the N⁺ species (pink shaded box), intermediate-ionization by the S⁺² species (yellow shaded box), and high-ionization by the O⁺² species (green shaded box). However, observations of J104457, J141851, and other EELGs probe an extended range of gas ionization phase that is capable of, for instance, emitting nebular O⁺³ (O IV $\lambda\lambda$ 1401,1404,1407), C⁺³ (C IV $\lambda\lambda$ 1548,1550), He⁺² (He II λ 1640), N⁺³ [N IV] $\lambda\lambda$ 1483,1487, and Ar⁺³ ([Ar IV] $\lambda\lambda$ 4711,4740). We, therefore, attempt to better characterize the very high-ionization nebulae of EELGs by establishing a four-zone ionization model with the addition of a very high-ionization zone defined by the He⁺² species (blue shaded box). Additional T_e and n_e diagnostic species are denoted by a color-coded outline for each ionization zone. Bottom: ionization potential energies, same as the top plot, but limited to species that are commonly observed in UV and optical spectra of H II regions in EELGs. The purple shaded boxes highlight the components of the O⁺²/O⁺ ratio that is commonly used as a diagnostic of the ionization parameter for the three-zone nebula model. In comparison, for EELGs, we recommend using the S⁺²/S⁺ ratio to probe the ionization parameter of the low- to intermediate-ionization zones and the Ar⁺³/Ar⁺² ratio to probe the high- to very high-ionization zones.

respectively. Together these three zones are able to adequately characterize the H $\scriptstyle\rm II$ regions of typical star-forming galaxies. For example, $\rm O^+$ and $\rm O^{+2}$ nicely span the entire ionization

energy range of the three-zone nebula model and so are commonly used as a ratio that is diagnostic of the ionization parameter. However, several of the important emission lines in our EELGs lie outside the high-ionization zone at even greater energies (i.e., C⁺³, He⁺², O⁺³, Ne⁺², and Ar⁺³) such that their contributions to the ionization structure and abundances of these galaxies are missing.

The presence of He II λ 1640, C IV $\lambda\lambda$ 1548,1550, and O IV $\lambda\lambda 1401,1404,1407$ emission lines in the HST/COS UV spectra in Figure 2, as well as [Ne III] λ 3869, Fe V λ 4227, He II λ 4686, and [Ar IV] $\lambda\lambda 4711,4740$ emission lines in the LBT/MODS optical spectra in Figure 3, reveal the interesting detection of a very high-ionization zone region within these EELG nebulae. We, therefore, attempt to better characterize the very highionization nebulae of EELGs by defining a *four-zone* ionization model. The four-zone model simply extends the classical threezone model with the addition of a very high-ionization zone that is designated by the He⁺² species (needed to produce the observed He II emission via recombination). In the bottom panel of Figure 4 we see that the [O III] $\lambda 5007/[O II] \lambda 3727$ ratio, which is commonly used as a proxy for ionization parameter in a three-zone nebula model, does not adequately characterize the full nebula of these EELGs, missing the very high-ionization zone in particular.

Alternatively, for EELGs, we recommend defining two additional ionization parameters to characterize the low-ionization and high-ionization volumes separately. Expanding on the works of Berg et al. (2016) and Berg et al. (2019b), we re-computed the temperature and density structure of J104457 and J141851 (Section 3.2.1), as well as the ionization structure (Section 3.2.2) and chemical abundances (Section 4), incorporating the new UV and optical emission lines measured in this work and considering the four-zone ionization model proposed here. To perform these calculations, we used the PYNEB package in PYTHON (Luridiana et al. 2012, 2015) with the atomic data adopted in Berg et al. (2019b).

3.1.1. Photoionization Models

To aid in our interpretation of the four-zone ionization model, we employed a spherical nebula model composed of nested spheres of decreasing ionization, which is supported by the visual compactness and structural simplicity of these galaxies (see Figure 1). Additionally, we ran new photoionization models, which were especially useful for testing ionization correction factors and understanding the ionization structure of J104457 and J141851.

Our photoionization models consist of a CLOUDY 17.00 (Ferland et al. 2013) grid assuming a simple, spherical geometry and a full covering factor of 1.0. For our central input ionizing radiation field, we use the "Binary Population and Spectral Synthesis" (BPASSv2.14; Eldridge & Stanway 2016; Stanway et al. 2016) single-burst models. Appropriate for EELGs, our grid covers a range of ages: $10^{6.0} - 10^{7.0}$ yr for our young bursts, ionization parameters: $-3.0 < \log U < -1.0$, matching stellar and nebular metallicities: $Z_{\star} = Z_{\text{neb}} = 0.001$, 0.002, 0.004, 0.006 = 0.05, 0.10, 0.20, $0.30 \, \mathrm{Z_{\odot}}$ (or $7.4 < 12 + \log(\mathrm{O/H})$ < 8.2), and densities: $n_e = 10^1 - 10^4 \, \mathrm{cm}^{-3}$. The Grevesse et al. (2010) solar abundance ratios and Orion grain set were used to initialize the relative gas-phase and dust abundances. These abundances were then scaled to cover the desired range in nebular metallicity, and relative C, N, and Si abundances $(0.25 < (X/O)/(X/O)_{\odot} < 0.75)$. The ranges in relative N/O, C/ O, and Si/O abundances were motivated by the observed values for nearby metal-poor dwarf galaxies (e.g., Garnett et al. 1995; van Zee & Haynes 2006; Berg et al. 2011, 2012, 2016, 2019b).

These CLOUDY models have a large number of zones (typically 200–300) that represent the number of shells or radial steps outward considered in the calculations. It is important to note that these zones or shells are physically different than the three- and four-zone ionization models discussed throughout this work. Specifically, the three- and four-zone ionization models are defined by the ionization potential energies of the representative ions, where each ionization zone is composed of many CLOUDY shells.

3.2. Measuring the Structure of Nebular Properties

Detailed abundance determinations from collisionally excited lines require knowledge of the electron temperature (T_e) and density (n_e) structure in a galaxy such that the nebular physical conditions are known for each ionic species. In the standard three-zone model, the most common method uses the T_e -sensitive [O III] $\lambda 4363/\lambda 5007$ ratio to directly calculate the electron temperature of the high-ionization gas. The temperatures of the low- and intermediate-ionization zones are then inferred from photoionization model-based relationships. In contrast, the density structure across ionization zones is more difficult to determine. Therefore, the three-zone model usually assumes a single, uniform density derived from the n_e -sensitive [S II] λ 6717/ λ 6731 ratio of the low-ionization zone. H II regions commonly have [SII] ratios that are consistent with the low density upper limit, where even large fluctuations on the order of 100% would have negligible impact on abundance calculations, and thus motivates the assumption of a homogeneous density distribution of $n_e = 100 \,\mathrm{cm}^{-3}$ throughout nebulae.

3.2.1. Temperature and Density Structure

Given the extreme nature of our EELGs, the simple three-zone model structure cannot be assumed. Fortunately, owing to the improved resolution and S/N of the LBT/MODS spectra over existing optical spectra, we were able to directly probe the physical conditions across the entire ionization energy range of J104457 and J141851. Specifically, we use different electron temperature and density measurements for each of the four ionization zones:

Low-ionization zone: we measure temperatures from the [O II] $\lambda\lambda7320,7330/\lambda\lambda3727,3729$ ratio and density from [S II] $\lambda6717/\lambda6731$. The [N II] $\lambda5755/\lambda\lambda6548,6584$ line ratio has been demonstrated to be a more robust measure of the electron temperature in the low-ionization zone (e.g., Berg et al. 2015), but the low N⁺ abundances of our EELGs precluded detection of the T_e -sensitive [N II] $\lambda5755$ auroral line.

Intermediate-ionization zone: we use the [S III] $\lambda 6312/\lambda 9069,9532$ ratio, after checking for atmospheric contamination of the red [SIII] lines to determine the intermediate-ionization zone temperature. Unfortunately, we do not have a robust probe of the density in this zone, but we are able to use the Si III] $\lambda 1883/\lambda 1892$ ratio from the archival low-resolution HST/COS spectra to measure an upper limit on the density in the low- to

II Using PYNEB, the theoretical ratio of emissivities of [S III] $\lambda 9532/\lambda 9069$ is $\epsilon_{\lambda 9532}/\epsilon_{\lambda 9069} = 2.47$, and remains consistent over a wide range of nebular temperatures (0.5 × 10⁴ $\lesssim T_e \lesssim 2.0 \times 10^4$) and densities (10² $\lesssim n_e \lesssim 10^4$). For J141851, [S III] $\lambda 9532/\lambda 9069 = 2.48$, consistent with the theoretical ratio. However, for J104457, [S III] $\lambda 9532/\lambda 9069 = 2.37$, and so [S III]

intermediate-ionization zone. We note that the optical [Cl III] $\lambda 5517/\lambda 5537$ line ratio is an excellent probe of the intermediate-ionization zone, however, these lines are too faint and lie too close to the dichroic to get adequate measurements from the LBT/MODS spectra.

High-ionization zone: we use the standard [O III] $\lambda 4363/\lambda 4959,5007$ ratio for the high-ionization zone temperature. While we also lack a strong probe of the density in the high-ionization zone, we estimate the C III] density using the $\lambda 1907/\lambda 1909$ ratio from the archival low-resolution HST/COS spectra, where C⁺² spans intermediate- to high-ionization energies.

Very high-ionization zone: with the very high-ionization zone defined by He⁺² (>54.42 eV) in Figure 4, the only pure very high-ionization emission lines we observe are He II, O IV, and [Fe V]. Therefore, in order to characterize the very high-ionization zone, we also consider bridge ions, or ions that partially span both the high- and very highionization zones, such as Ne⁺² (40.96–63.45 eV) and Ar⁺ (40.74-59.81 eV). Specifically, we use the temperaturesensitive [Ne III] $\lambda 3342/\lambda 3868$ ratio and the densitysensitive [Ar IV] $\lambda 4711/\lambda 4740$ ratio. Note that at the resolution of the LBT/MODS spectra, the [Ar IV] λ 4711 line is blended with He I λ 4713. To correct for the He I flux contribution, we first continuum subtract the spectra to account for He I absorption and then estimate the He I $\lambda4713$ flux from the measured He I $\lambda4471$ flux and the theoretical He I $\lambda 4713/\lambda 4471$ ratio.

The temperatures and densities determined for each of the four ionization zones are listed in Table 3. Assuming a simple high-to-low ionization gradient from center-to-edge of the nebula, all of the measurements together describe an HII region with higher temperatures and densities in the center that decrease with distance outward. Comparing the extremes of the temperatures and densities across the different zones, J104457 has gradients spanning $\Delta T_e = 1500~{\rm K}$ and $\Delta n_e = 1350~{\rm cm}^{-3}$, while the gradients of J141851 are somewhat steeper with $\Delta T_e = 9000~{\rm K}$ and $\Delta n_e = 2040~{\rm cm}^{-3}$. Note, however, that several of the temperature and density measurements have significant uncertainties.

Within these measured temperature ranges, the high- and very high-ionization zones of the J104457 nebula have temperatures that are consistent with one another and are roughly a thousand K hotter than the outer region of the low- to intermediateionization zones (weighted average $T_e = 17,840 \,\mathrm{K}$). We note that the [O II] temperature is consistent with the higher, central temperatures, but [O II] measurements are often systematically biased to hotter temperatures (e.g., Esteban et al. 2009; Pilyugin et al. 2009; Berg et al. 2020). For J141851, the intermediate- and high-ionization zones within the nebula have temperatures that are consistent with one another within the errors and are a few thousand K hotter than the outer low-ionization region. In comparison to the very high-ionization zones, however, the intermediate-ionization zones of both nebula are \sim 1500–5600 K cooler. These temperature and density structures, paired with our assumed spherical ionization model, suggest extreme radiation sources are at the center of these EELGs.

3.2.2. Characterizing the Ionization Parameter

An important parameter for characterizing the physical nature of an H II region is the ionization parameter, q, or the

Table 3
Three-zone and Four-zone Nebular Conditions for EELGs

	Ion. Zone	J104457	J141851
Property	3 Zone 4 Zone	3 Zone 4 Zone	3 Zone 4 Zone
T_e [Ne III] (K)	VH	$19,\!200 \pm 2,\!300$	$23,600 \pm 3,200$
T_e [O III] (K)	H	$19,200 \pm 200$	$17,800 \pm 200$
T_e [S III] (K)	I	$17,700 \pm 500$	$18,000 \pm 1,200$
T_e [O II] (cm ⁻³)	L	$19,100 \pm 1,500$	$14,600 \pm 600$
ΔT_e (K)		1,500	9,000
n_e [Ar IV] (cm ⁻³)	VH	$1,550 \pm 1,100$	$2,110 \pm 1,300$
n_e C III] (cm ⁻³)	$H\!\!-\!\!L$	+<8,870	+<1,680
n_e Si III] (cm ⁻³)	I–L	+<9,450	+<3,610
n_e [S II] (cm ⁻³)	L	200 ± 40	70 ± 40
$\Delta n_e \; (\text{cm}^{-3})$		1,350	2,040
$\log U_{\rm low}$	I/L	$N/A \mid -2.65$	$N/A \mid -2.66$
([S III]/[S II])			
$\log U_{\rm int}$	All L/H	$-1.77 \mid -1.77$	$-2.42 \mid -2.42$
([O III]/[O II])	, ,	'	·
$\logU_{ m high}$	N/A VH/H	$N/A \mid -1.51$	$N/A \mid -1.31$
([Ar IV]/[Ar III])	, , ,	, .	, .
$\Delta \log U$	All	-1.14	-1.35
$\log U_{ m ave}$	All	-1.77 -1.66	-2.42 -1.93

Note. Nebular temperatures, densities, and ionization parameters for J104457 and J141851 using both the three-zone and four-zone models. Column 2 specifies the ionization zone(s) of each property, where L=low, I=intermediate, H=high, $VH=very\ high$, and $All=all\ ionization\ zones$. Temperatures and densities from ions spanning different ionization zones are given first, followed by ionization parameters derived from three different line ratios

flux of ionizing photons (cm⁻² s⁻¹) per volume density of H, $n_{\rm H}$ (cm⁻³). More commonly, we use the dimensionless log U ionization parameter, defined as U = q/c. While U varies as a function of radius throughout a nebula, decreasing as the number of ionizing photons is geometrically diluted further from the central source, in practice we typically characterize a nebula by its volume-averaged ionization parameter, U_{ave} . In a classic photoionization model, log U_{ave} is determined as a function of the observed light-weighted optical [O III] $\lambda 5007/$ [O II] λ 3727 ratio, or the degree of ionization of oxygen. This is a reasonable quantity for typical star-forming HII regions, where the variation in $\log U$ across the nebulae declines gradually as a function of radius (see further discussion in Section 5.4) and has an average value of $-3.2 < \log U < -2.9$ (e.g., Dopita et al. 2000; Moustakas et al. 2010). For J104457 and J141851, we use the equations from Berg et al. (2019b; see Table 3) with the observed [O III] $\lambda 5007/[O II] \lambda 3727$ ratios to determine ionization parameters for the three-zone model of log $U_{\text{ave}} = -1.77$, -2.42, respectively. Note, these ionization parameters are not only atypical compared to local populations of galaxies, but are also likely underestimated, as the O⁺ and O⁺² ions do not characterize the full extent of the very highionization zone in EELGs (see Figure 4).

To better characterize the extreme, extended ionization parameter space of the nebular environments of EELGs, we recommend examining how the ionization parameter changes across ionization zones. In this context, the standard three-zone log $U_{\rm ave}$ is best equated with the intermediate-ionization zone, log $U_{\rm int}$, but two additional ionization parameters are needed to represent the low-ionization and high-ionization volumes separately. We use the photoionization models described in Section 3.1.1 to estimate new ionization parameters to

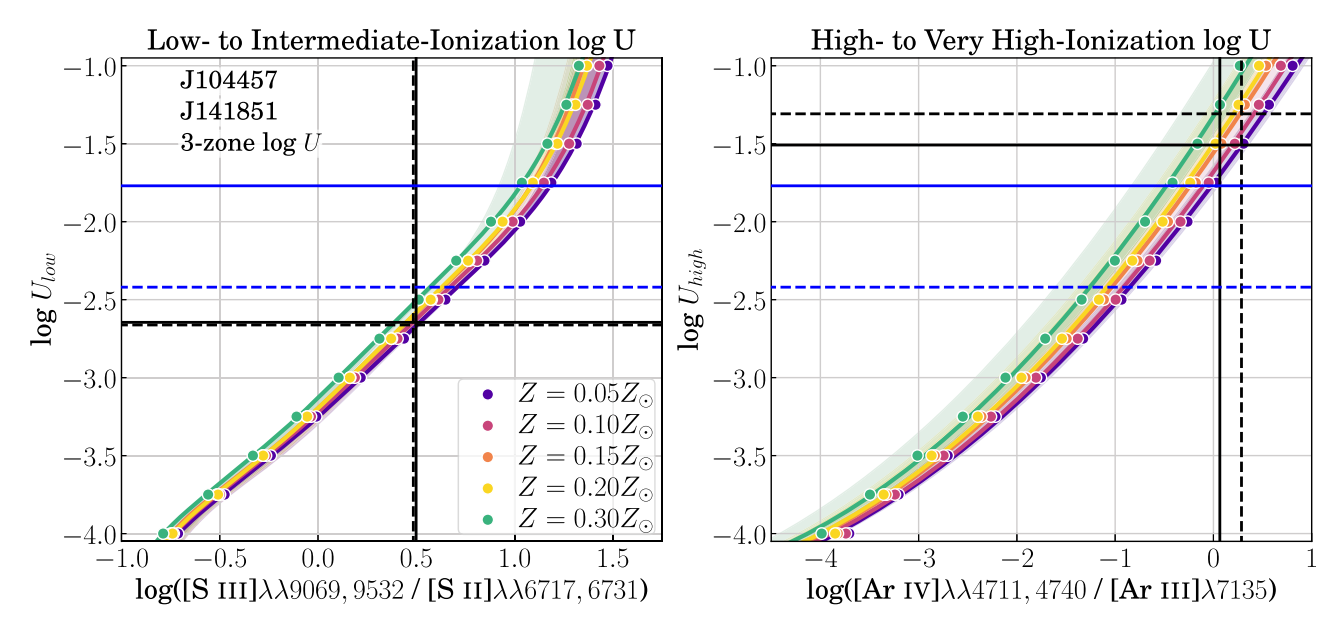


Figure 5. Photoionization models characterizing ionization parameter in different parts of a nebula. Models of a given metallicity (indicated by color) are shown for a burst age of $10^{6.7}$ yr (solid line) and spanning $10^6 - 10^7$ yr (shaded regions). Left: the low- and intermediate-ionization zones can be characterized by the [S II] $\lambda\lambda671\overline{7}$,31 and [S III] $\lambda\lambda9069$,32 emission lines, whose ionization energies span these zones. Right: the [Ar III] $\lambda7135$ and [Ar IV] $\lambda\lambda4711$,40 emission lines can be used to characterize the high- to very high-ionization zone, as the ionization energy range of [Ar IV] extends beyond the classical three-zone model and into the very high-ionization zone. Using the [S III]/[S II] ratio, the log U_{low} values inferred for J104457 and J141851 are lower than their corresponding three-zone log U_{int} values determined from [O III]/[O II]. On the other hand, $\log U_{\rm high}$ values inferred from the [Ar IV]/[Ar III] ratios are considerably higher than the three-zone $\log U_{\rm int}$ values.

characterize the low- to intermediate-ionization volume, $\log U_{\rm low}$, as a function of the [S III] $\lambda\lambda9069,9532/[S II]$ $\lambda\lambda6717,6731$ emission-line ratio and the high- to very high-ionization volume, log U_{high} , as a function of the [Ar IV] $\lambda\lambda4711,4740/[\text{Ar III}]$ $\lambda 7135$ emission-line ratios. To summarize, we determine the ionization structure with the following relations:

- 1. log $U_{\rm low}\propto$ [S III] $\lambda\lambda9069,9532/$ [S II] $\lambda\lambda6717,6731$ 2. log $U_{\rm int}\propto$ [O III] $\lambda5007/$ [O II] $\lambda3727$
- 3. $\log U_{\rm high} \propto [{\rm Ar\,IV}] \, \lambda \lambda 4711,4740/[{\rm Ar\,III}] \, \lambda 7135$

Note that all three of these diagnostic ratios utilize the same element and so are not vulnerable to variations in relative abundances.

Our log U_{low} versus [S III]/[S II] and log U_{high} versus [Ar IV]/ [Ar III] models are plotted in Figure 5. The light color shading depicts the minimal variation in the models with burst age, centered on models with an age of $t = 10^{6.7}$ yr (colored lines) and extending from $t = 10^{6.0} - 10^{7.0}$ yr. We fit each metallicity model with a polynomial of the shape: $y = c_3 \cdot x^2 + c_2 \cdot x + c_1$, where $y = \log U$, x is the log of the observed line ratio, and the c coefficients are listed in Table 4.

The observed [SIII]/[SII] line ratios of J104457 (black solid line) and J141851 (black dashed line) are nearly the same, resulting in measured ionization parameter values of log $U_{low} = -2.65$, -2.66 that are lower than the standard three-zone [O III]/[O II]derived volume-averaged values (blue lines; $\log U_{ave} = -1.77$, -2.42). For the [Ar IV]/[Ar III] line ratios, we measured log $U_{\rm high}$ values of -1.51, -1.31 for J104457 and J141851, respectively, that are higher than the three-zone $\log U_{\text{ave}}$ values.

4. Abundance Determinations

We compute absolute and relative abundances for J104457 and J141851 with both the standard three-zone ionization

model and the expanded four-zone ionization model. For all calculations, we use the PYNEB package in PYTHON with the atomic data adopted in Berg et al. (2019a) for a five-level atom model, plus a six-level atom model for oxygen in order to utilize the UV O III] $\lambda\lambda 1661,1666$ lines for C/O abundance determinations. Ionic abundances were calculated from the optical spectra for O^0/H^+ , O^+/H^+ , O^{+2}/H^+ , N^+/H^+ , S^+/H^+ , S^{+2}/H^+ , Ar^{+2}/H^+ , Ar^{+3}/H^+ , Ne^{+2}/H^+ , Fe^{+2}/H^+ , Fe^{+3}/H^+ , and Fe^{+4}/H^+ , whereas the C^{+2}/O^{+2} , O^{+3}/O^{+2} , and S^{+3}/O^{+2} relative abundances were determined from the UV spectra.

To determine accurate ionic abundances, we adopt the characteristic temperature and density of each ionization species when available (see Section 3.2.1). Specifically, we adopt the $T_e[O II]$ temperature and $n_e[S II]$ density for the lowionization zone ions: O^0 , O^+ , N^+ , S^+ , N^+ , and Fe^{+2} . For the intermediate-ionization zone ions, S^{+2} and Ar^{+2} , we adopt the $T_e[S III]$ temperature. However, owing to their large uncertainties, we do not use either of the intermediate-ionization zone densities (n_e C III], n_e Si III]), but rather adopt the n_e [S II] density. For the high-ionization O⁺², C⁺², S⁺³, and Fe⁺³ ions, we use the $T_e[O III]$ temperature and $n_e[Ar IV]$ very highionization density. Finally, we use the $T_e[\text{Ne III}]$ temperature and $n_e[Ar IV]$ density to characterize the very high-ionization zone and calculate O⁺³ and Fe⁺⁴. Note, Ne⁺² and Ar⁺³ partially span both the high- and very high-ionization zones, and so an average of the temperatures and densities characterizing these zones is used.

In general, the total abundance of an element relative to hydrogen in an HII region is calculated by summing the abundances of the individual ionic species together relative to hydrogen as:

$$\frac{N(X)}{N(H)} = \sum_{i} \frac{N(X^{i})}{N(H^{+})} = \sum_{i} \frac{I_{\lambda(i)}}{I_{H\beta}} \frac{j_{H\beta}}{j_{\lambda(i)}}, \qquad (1)$$

Table 4
Coefficients for Ionization Parameter Model Fits

	$Z(Z_{\odot})$					
y = f(x)	0.005	0.05	0.10	0.20	0.30	0.40
$y=\log U_{low}$:						
$x = \log([S III]/[S II])$						
<i>c</i> ₁	-3.2705	-3.2506	-3.2204	-3.1963	-3.1295	-3.1147
<i>c</i> ₂	1.1163	1.1145	1.1397	1.1811	1.2104	1.2280
<i>c</i> ₃	0.1692	0.2060	0.2154	0.2236	0.1844	0.1816
$y = log U_{high}$:						
$x = \log([Ar IV]/[Ar III])$						
c ₁	-1.9370	-1.6396	-1.4934	-1.2273	-0.9737	-0.7817
<i>c</i> ₂	0.7662	0.8589	0.9093	0.9695	1.0210	1.0545
<i>c</i> ₃	0.0554	0.0658	0.0711	0.0741	0.0760	0.0769

Note. CLOUDY photoionization model fits of the form $f(x) = c_3 \cdot x^2 + c_2 \cdot x + c_1$ for the ionization parameters characterizing the ionization parameter. For the low-to intermediate-ionization region, log U_{low} is determined from $x = \log([\text{S III}] \lambda\lambda 9069,9532/[\text{S II}] \lambda\lambda 6717,6731)$ and for the high- to very high-ionization region, log U_{high} is determined from $x = \log([\text{Ar IV}] \lambda\lambda 4711,4740/[\text{Ar III}] \lambda7135)$. The best fits are for a burst of star formation with an age of $t = 10^{6.7}$ yr. The model grids and polynomial fits are shown in Figure 5.

where the emissivity coefficients, $j_{\lambda(i)}$, are determined for the appropriate ionization zone temperature and density. Details of elemental abundance determinations are given below.

4.1. Ionic and Total O Abundances

The most common method of calculating O/H abundances involves adding together the dominant ionic abundances, O⁺/H⁺ and O⁺²/H⁺, determined from the [O II] $\lambda 3727$ and [O III] $\lambda \lambda 4959,5007$ emission lines. Because the ionization energy ranges of O⁺ and O⁺² span the full range of a standard three-zone H II region, contributions from O⁰ and O⁺³ (and higher ionization species) can be ignored. In our four-zone ionization model this is not necessarily the case. For J104457 and J141851 we detect weak O IV $\lambda\lambda 1401,1405,1407^{12}$ emission in their HST/COS spectra and so can directly estimate the impact of O⁺³ on the total O abundance. To do so, we calculated O⁺³/H⁺ = [O⁺³/O⁺²]_{UV}/[O⁺²/H⁺]_{opt.}, where the O⁺³/O⁺² abundance was determined from the UV O IV $\lambda\lambda 1401,1407/O$ III] $\lambda 1666$ ratio. We also detect O I $\lambda\lambda 6300,6363$ emission in the LBT/MODS spectra, allowing a measure of the O⁰/H⁺ abundance. Therefore, the total oxygen abundances (O/H) were calculated from the sum of four ionization species:

$$\frac{O}{H} = \frac{O^0}{H^+} + \frac{O^+}{H^+} + \frac{O^{+2}}{H^+} + \frac{O^{+3}}{H^+}.$$
 (2)

Ionic and total O/H abundances determined for both the classical three-zone and expanded four-zone ionization models are reported in Table 5. The main differences are the inclusion of the $\rm O^0$ and $\rm O^{+3}$ species and the use of the very high-ionization zone density for species in the high-ionization zone in the four-zone model. In general, we find that the $\rm O^{+3}/H^+$ abundances are very small, with the $\rm O^{+3}/O_{tot}$ fractions of only 1–2%. Additionally, the effects of the different density assumptions in the three-zone versus four-zone model, where the density was increased from $\sim \! 10^2$ to $\sim \! 10^3 \, \rm cm^{-3}$, are negligible. In fact, the $\rm O^{+2}/H^+$ abundances differ by much less than 1%.

4.2. Ionization Correction Factors

If all of the species of an element present in the H II region are not observed, then an ionization correction factor (ICF) must be used to account for the missing abundance. We showed in the previous section that, even for EELGs, the rarely observed higher ionization species of O (above O^{+2}) represent a small fraction of the total O abundance, and so, total O abundances can still be accurately determined by the simple sum of the O^+/H^+ and O^{+2}/H^+ ratios. The other elements discussed here, namely N, C, S, Ar, Ne, and Fe, can have significant fractions of their species in unobserved ionic states and so require an ICF to infer their total abundances.

For each element, we determined appropriate ICFs based on photoionization modeling as a function of ionization parameter. For the three-zone model, we adopted the [O III]/[O II]-based log $U_{\rm ave}$ to determine the appropriate ICFs. We then determined a comparable volume-averaged ionization parameter to characterize the four-zone model from the set of ionization parameters determined in Section 3.2.2. To do so, we calculated the average ionization parameter, log $U_{\rm ave}$, by weighting the log $U_{\rm low}$, log $U_{\rm int}$, and log $U_{\rm high}$ values by their corresponding ionization fractions of oxygen, as determined in Section 4.1. For J104457 and J141851, we measure log $U_{\rm ave} = -1.70$, -1.91, respectively, for the four-zone model and use these values to determine the appropriate ICFs.

4.3. N/O Abundances

Relative N/O abundances are often determined by employing the simple assumption that N/O = N⁺/O⁺. This method benefits from the similar ionization and excitation energies of N⁺ and O⁺ (see Figure 4), and is particularly useful for low to moderate ionization-dominated nebulae. For high-ionization nebulae, a N ICF is needed to correct N abundances for higher ionization species of N, where N/H = ICF(N⁺) × N⁺/H⁺. Several N ICFs in the literature have been derived as a function of O⁺/(O⁺ + O⁺²) = O⁺/O_{tot.} (e.g., Peimbert & Costero 1969; Izotov et al. 2006; Nava et al. 2006; Esteban et al. 2020); here we consider two of them. First, we calculate the simple N ICF from Peimbert & Costero (1969): ICF(N+) = O_{tot.}/O⁺, and then consider the recent empirical fit from Esteban et al. (2020) to Milky Way data: ICF(N⁺) = 0.39+1.19 × (O_{tot.}/O⁺). Note that these methods require a calculation of an ionic and total O

 $^{^{12}}$ Note that the emission line at 1405 Å is a blend of O IV λ 1404.806 and S IV λ 1404.808, and so is not used here.

 Table 5

 Three-zone and Four-zone Ionic and Total Abundances for EELGs

0"/H" (10") N/A L		Ion. Zone	J104457	J141851
0 ' 11 (10 °)	Property	3 Zone 4 Zone	3 Zone 4 Zone	3 Zone 4 Zone
0 - 2 H 10 - 6		N/A L	0.22 ± 0.05	0.84 ± 0.12
0-7)H (10-6) N/A VH N/A 0.011 ± 0.001 N/A VH N/A 1.1± 0.6 N/A 0.072 Hz, v (0.6) N/A VH N/A 1.1± 0.6 N/A 0.079 Hz, v (0.6) N/A 0.079 0.020 0.007 0.020 0.007 0.020 0.007 0.020 0.007 0.020 0.007 0.020 0.008 0.007 0.020 0.075 0.020 0.075 0.020 0.075 0.020 0.075 0.070 0.020 0.075 0.070 0.075 0.070 0.075 0.070 0.075 0.070 0.075 0.070 0.075 0.070 0.075			1.14 ± 0.25	4.58 ± 0.67
$\begin{array}{c c c c c c c c c c c c c c c c c c c $		Н	27.0 ± 0.67	37.0 ± 0.94
0.008 0.007 0.020 0.0° O ₁		N/A VH	$N/A \mid 0.011 \pm 0.001$	$N/A \mid 0.013 \pm 0.001$
0 / 0/∞ 0 / 2/O _{0c} 0 / 2/O _{0c} 0 / 3/O ₀		N/A VH	$N/A \mid 1.1 \pm 0.6$	$N/A \mid 0.62 \pm 0.70$
0.72 O _{cs}			0.008 0.007	0.020 0.019
O°2 O _{loc} N/A 0.037 N/A 12 + log(O/H)(H) All 7.44 ± 0.01 7.44 ± 0.01 7.62 ± 0.01 12 + log(O/H)(H) All N/A 7.47 ± 0.03 N/A (O/H)(O/H) _S All 0.056 ± 0.002 0.088 ± 0.003 0.084 ± 0.003 C°2 O°2 H 0.174 ± 0.037 0.186 ± 0.041 0.147 ± 0.035 0.066 ± 0.000 0.088 ± 0.003 0.084 ± 0.003 log(C/O) All 0.75 ± 0.09 0.073 ± 0.09 0.73 ± 0.09 0.73 ± 0.09 0.73 ± 0.09 0.73 ± 0.09 0.73 ± 0.09 0.73 ± 0.09 0.022 ± 0.005 0.088 ± 0.001 0.088 ± 0.001 0.022 ± 0.005 0.088 ± 0.001 0.022 ± 0.005 0.024 ± 0.002 0.024 ± 0.002	${ m O}^+/{ m O}_{ m tot.}$		0.040 0.038	0.108 0.104
O°2 O _{loc} N/A 0.037 N/A 12 + log(O/H)(H) All 7.44 ± 0.01 7.44 ± 0.01 7.62 ± 0.01 12 + log(O/H)(H) All N/A 7.47 ± 0.03 N/A (O/H)(O/H) _S All 0.056 ± 0.002 0.088 ± 0.003 0.084 ± 0.003 C°2 O°2 H 0.174 ± 0.037 0.186 ± 0.041 0.147 ± 0.035 0.066 ± 0.000 0.088 ± 0.003 0.084 ± 0.003 log(C/O) All 0.75 ± 0.09 0.073 ± 0.09 0.73 ± 0.09 0.73 ± 0.09 0.73 ± 0.09 0.73 ± 0.09 0.73 ± 0.09 0.73 ± 0.09 0.022 ± 0.005 0.088 ± 0.001 0.088 ± 0.001 0.022 ± 0.005 0.088 ± 0.001 0.022 ± 0.005 0.024 ± 0.002 0.024 ± 0.002	$O^{+2}/O_{tot.}$		0.952 0.917	0.872 0.862
$\begin{array}{c ccccccccccccccccccccccccccccccccccc$	$O^{+3}/O_{tot.}$		N/A 0.037	N/A 0.015
$\begin{array}{c c c c c c c c c c c c c c c c c c c $		All	7.44 ± 0.01 7.44 ± 0.01	$7.62 \pm 0.01 \mid 7.62 \pm 0.02$
$\begin{array}{c c c c c c c c c c c c c c c c c c c $	$12 + \log(O/H)_{UV}$	All	$N/A \mid 7.47 \pm 0.03$	N/A 7.63 ± 0.02
$ \begin{array}{c ccccccccccccccccccccccccccccccccccc$		All	$0.056 \pm 0.002 \mid 0.058 \pm 0.003$	$0.084 \pm 0.003 \mid 0.087 \pm 0.004$
$ \begin{array}{c ccccccccccccccccccccccccccccccccccc$		Н	•	$0.147 \pm 0.035 \mid 0.169 \pm 0.037$
$\begin{array}{c ccccccccccccccccccccccccccccccccccc$				0.960 ± 0.200 1.095 ± 0.201
$ \begin{array}{c c c c c c c c c c c c c c c c c c c $		All	•	-0.83 ± 0.09 -0.77 ± 0.09
$\begin{array}{c ccccccccccccccccccccccccccccccccccc$				$0.022 \pm 0.005 \mid 0.027 \pm 0.006$
$\begin{array}{c ccccccccccccccccccccccccccccccccccc$				14.4 ± 1.4
$\begin{array}{c c c c c c c c c c c c c c c c c c c $		_		$6.232 \pm 0.929 \mid 15.950 \pm 2.338$
$\begin{array}{c c c c c c c c c c c c c c c c c c c $	* /		·	9.626 ± 1.430
$ \begin{array}{c ccccccccccccccccccccccccccccccccccc$	' / '			11.845 ± 0.100
$\begin{array}{c ccccccccccccccccccccccccccccccccccc$		All		$5.95 \pm 0.07 \mid 6.37 \pm 0.07$
$\begin{array}{c ccccccccccccccccccccccccccccccccccc$	• , , .		•	6.14 ± 0.07
$\begin{array}{c ccccccccccccccccccccccccccccccccccc$				6.23 ± 0.04
$ \begin{array}{c ccccccccccccccccccccccccccccccccccc$				-1.48 ± 0.07
$\begin{array}{c ccccccccccccccccccccccccccccccccccc$	C . , ,			$-1.66 \pm 0.07 \mid -1.26 \pm 0.07$
$ \begin{array}{c ccccccccccccccccccccccccccccccccccc$			•	-1.49 ± 0.07
$ \begin{array}{c ccccccccccccccccccccccccccccccccccc$				-1.39 ± 0.04
$ \begin{array}{c ccccccccccccccccccccccccccccccccccc$	•			$0.013 \pm 0.002 \mid 0.035 \pm 0.006$
$ \begin{array}{c ccccccccccccccccccccccccccccccccccc$			•	0.021 ± 0.002
$\begin{array}{c ccccccccccccccccccccccccccccccccccc$				0.026 ± 0.002
$\begin{array}{c ccccccccccccccccccccccccccccccccccc$				0.77 ± 0.09
$\begin{array}{cccccccccccccccccccccccccccccccccccc$				3.56 ± 0.39
$ \begin{array}{c ccccccccccccccccccccccccccccccccccc$				1.58 ± 3.33
$\begin{array}{c ccccccccccccccccccccccccccccccccccc$				$1.101 \pm 0.164 \mid \ 1.351 \pm 0.198$
$\begin{array}{c ccccccccccccccccccccccccccccccccccc$			•	2.383 ± 0.238
$ \begin{array}{c ccccccccccccccccccccccccccccccccccc$		All		$5.68 \pm 0.07 \mid 5.77 \pm 0.06$
$\begin{array}{c ccccccccccccccccccccccccccccccccccc$	- · · ·			5.77 ± 0.19
$\begin{array}{c ccccccccccccccccccccccccccccccccccc$				6.01 ± 0.05
$\begin{array}{c ccccccccccccccccccccccccccccccccccc$	0, ,,			$-1.94 \pm 0.07 \mid -1.86 \pm 0.06$
$\begin{array}{c ccccccccccccccccccccccccccccccccccc$			•	$N/A \mid -1.86 \pm 0.19$
$ \begin{array}{cccccccccccccccccccccccccccccccccccc$				-1.62 ± 0.05
$ \begin{array}{cccccccccccccccccccccccccccccccccccc$				$0.036 \pm 0.006 \mid 0.045 \pm 0.006$
$ \begin{array}{c ccccccccccccccccccccccccccccccccccc$			·	$0.045 \pm 0.021 \mid 0.045 \pm 0.006$
$\begin{array}{cccccccccccccccccccccccccccccccccccc$, .	0.079 ± 0.008
$\begin{array}{c ccccccccccccccccccccccccccccccccccc$				7.86 ± 0.99
$\begin{array}{cccccccccccccccccccccccccccccccccccc$				$16.6 \pm 0.60 \mid 11.0 \pm 2.90$
$\begin{array}{cccccccccccccccccccccccccccccccccccc$			·	$1.062 \pm 0.158 \mid 1.021 \pm 0.150$
$\begin{array}{cccccccccccccccccccccccccccccccccccc$			•	1.013 ± 0.101
$\begin{array}{c ccccccccccccccccccccccccccccccccccc$		All		$5.41 \pm 0.05 \mid 5.29 \pm 0.11$
$\begin{array}{c ccccccccccccccccccccccccccccccccccc$				$5.39 \pm 0.04 \mid 5.28 \pm 0.11$
$\begin{array}{c ccccccccccccccccccccccccccccccccccc$	***			$-2.20 \pm 0.05 \mid -2.35 \pm 0.12$
$ \begin{array}{cccccccccccccccccccccccccccccccccccc$			•	$-2.22 \pm 0.04 \mid -2.35 \pm 0.12$
$ \begin{array}{cccccccccccccccccccccccccccccccccccc$			•	$0.104 \pm 0.012 \mid 0.077 \pm 0.013$
$\begin{array}{cccccccccccccccccccccccccccccccccccc$			•	$0.099 \pm 0.008 \mid 0.076 \pm 0.012$
$ \begin{array}{cccccccccccccccccccccccccccccccccccc$			•	$6.29 \pm 0.22 \mid 4.37 \pm 0.11$
$ \begin{array}{cccccccccccccccccccccccccccccccccccc$		11 411		$0.29 \pm 0.22 \mid 4.37 \pm 0.11$ $1.156 \pm 0.172 \mid 1.049 \pm 0.154$
$12 + log(Ne/H) \hspace{1.5cm} All \hspace{1.5cm} 6.66 \pm 0.10 \hspace{.1cm} \hspace{.1cm} 6.66 \pm 0.15 \hspace{1.5cm} 6.86 \pm 0.06 \hspace{.1cm} $			•	$1.130 \pm 0.172 \mid 1.049 \pm 0.134$ 1.117 ± 0.049
		Δ11		$6.86 \pm 0.06 \mid 6.66 \pm 0.14$
$17 \pm \log(Ne/H) (PC69)$ All $6.66 \pm 0.02 \pm 6.66 \pm 0.15$ $6.95 \pm 0.02 \pm 0.$	$12 + \log(Ne/H)$ $12 + \log(Ne/H)$ (PC69)	All	$6.66 \pm 0.10 \mid 6.66 \pm 0.15$	$6.85 \pm 0.03 \mid 6.00 \pm 0.14$ $6.85 \pm 0.03 \mid 6.39 \pm 0.13$
				$-0.75 \pm 0.03 \mid -0.97 \pm 0.15$
			·	$-0.75 \pm 0.03 \mid -0.97 \pm 0.13$ $-0.77 \pm 0.03 \mid -0.94 \pm 0.14$

Table 5 (Continued)

Property	Ion. Zone 3 Zone 4 Zone	J104457 3 Zone 4 Zone	J141851 3 Zone 4 Zone
(Ne/H)/(Ne/H) _⊙	All	$0.053 \pm 0.011 \mid 0.053 \pm 0.018$	$0.085 \pm 0.012 \mid 0.054 \pm 0.014$
(Ne/H)/(Ne/H) _⊙ (PC69)	All	$0.054 \pm 0.002 \mid 0.054 \pm 0.019$	$0.082 \pm 0.004 \mid 0.057 \pm 0.014$
$Fe^{+2}/H^+(10^{-8})$	L	2.81 ± 0.53	7.03 ± 0.36
$Fe^{+3}/H^{+}(10^{-8})$	Н	10.1 ± 3.60	26.1 ± 4.1
$Fe^{+4}/H^{+}(10^{-8})$	VH	$N/A \mid 0.20 \pm 0.08$	$N/A \mid 0.64 \pm 0.27$
$ICF(Fe^{+2})_1$		$15.783 \pm 1.051 \mid 20.083 \pm 2.132$	$3.996 \pm 0.595 \mid 10.292 \pm 1.508$
$ICF(Fe^{+2})_2$ (109)		36.098 ± 4.653	13.199 ± 1.961
$ICF(Fe^{+2,4})_3$		$N/A \mid 20.083 \pm 2.132$	$N/A \mid 10.292 \pm 1.508$
$ICF(Fe^{+2,3,4})_4$		$N/A \mid 1.005 \pm 0.107$	$N/A \mid 0.635 \pm 0.148$
$12 + \log(\text{Fe/H})_1$	All	$5.65 \pm 0.12 \mid 5.77 \pm 0.06$	5.42 ± 0.08 5.88 ± 0.08
12+log(Fe/H) ₂ (I09	All	$5.96 \pm 0.12 \mid 6.02 \pm 0.07$	$5.94 \pm 0.08 \mid 5.99 \pm 0.08$
$12 + \log(\text{Fe/H})_3$	All	$N/A \mid 5.80 \pm 0.06$	N/A 5.92 ± 0.08
12+log(Fe/H) ₄	All	$N/A \mid 5.08 \pm 0.18$	$N/A \mid 5.55 \pm 0.12$
$log(Fe/O)_1$	All	$-1.80 \pm 0.11 \mid -1.69 \pm 0.07$	$-2.19 \pm 0.08 \mid -1.75 \pm 0.08$
$log(Fe/O)_2$ (IO9)	All	-1.49 ± 0.12 -1.44 ± 0.08	-1.68 ± 0.08 -1.64 ± 0.08
$log(Fe/O)_3$	All	$N/A \mid -1.67 \pm 0.07$	$N/A \mid -1.72 \pm 0.08$
$log(Fe/O)_4$	All	$N/A \mid -2.38 \pm 0.19$	$N/A \mid -2.09 \pm 0.12$
$(Fe/H)_1/(Fe/H)_{\odot}$	All	$0.015 \pm 0.004 \mid 0.019 \pm 0.002$	$0.009 \pm 0.002 \mid 0.024 \pm 0.002$
$(Fe/H)_2/(Fe/H)_{\odot}(I09)$	All	$0.031 \pm 0.008 \mid 0.033 \pm 0.005$	$0.029 \pm 0.005 \mid 0.031 \pm 0.005$
(Fe/H) ₃ /(Fe/H) _⊙	All	$N/A \mid 0.020 \pm 0.003$	$N/A \mid 0.026 \pm 0.003$
(Fe/H) ₄ /(Fe/H) _⊙	All	$N/A \mid 0.004 \pm 0.002$	$N/A \mid 0.011 \pm 0.003$

Note. Ionic and total abundances for J104457 and J141851 using both the three- and four-zone models. Column 2 specifies the ionization zone(s) of each property, where L = low, I = intermediate, H = high, VH = very high, and All = all ionization zones. Abundances derived using an ICF from the literature are italicized. Abundances relative to solar are given using the following notation: $[X/H] = (X/H)/(X/H)_{\odot}$. Specific notes for each element are provided below. Oxygen: the four-zone O/H uses O^{+3}/H^+ , which was determined in two ways: (1) using the O^{+3}/O^{+2} ratio predicted from photoionization models (see Figure 9); (2) using the UV O IV $\lambda\lambda1401$,1407 line detections relative to O III] $\lambda1666$. Carbon: C/O was determined from the UV emission lines only. Nitrogen: N/H and N/O were determined using three different ICFs: (1) this work (see Figure 6); (2) Peimbert & Costero (1969); (3) Esteban et al. (2020). Sulfur: The corrections for missing ionization states for S/H and S/O were determined in three ways: (1) ICF from this work (see Figure 6); (2) using the UV S IV $\lambda1406$ line detection; (3) ICF from Thuan et al. (1995). Argon: Ar/H and Ar/O were determined using ICFs from: (1) this work (see Figure 6); (2) Thuan et al. (1995). Neon: Ne/H and Ne/O were determined using ICFs from: (1) this work (see Figure 6); (2) Peimbert & Costero (1969). Iron: Prover Prov

abundance, where $O_{tot.}$ is just the sum of O^+ and O^{+2} ions in the three-zone model. Therefore, we also use the photoionization models described in Section 3.1.1 to investigate a N ICF that can be inferred from observations of strong emission lines alone.

In the top panel of Figure 6 we plot our model N ICF versus log U for a range of metallicities. Here, the N ICF is the ionization fraction of N^+ , or $ICF(N^+) = N_{tot.}/N^+ = [X(N^+)]^{-1}$, and is used to correct N/H abundances as

$$\frac{N}{H} = \frac{N^+}{H^+} \times [X(N^+)]^{-1} = \frac{N^+}{H^+} \times ICF(N^+).$$

We use the average ionization parameter values of J104457 (solid line) and J141851 (dashed line) to determine their N ICFs in the 3 zone (blue lines) and four-zone (black lines) models. We find that our N ICFs are generally smaller than those of Peimbert & Costero (1969) and Esteban et al. (2020) for the three-zone model and larger or equivalent than these literature ICFs for the four-zone model. These differences are not unexpected given the two-zone model basis of the ${\rm O}^+/{\rm O}_{\rm tot.}$ variable and dissimilar calibration samples used in Peimbert & Costero (1969) and Esteban et al. (2020). Further, our models have an explicit benefit over the past models mentioned here: since a number of different emission-line ratio calibrations have been recommended to infer ionization parameter (see, e.g.,

Levesque & Richardson 2014; Berg et al. 2019b), our ICF models allow significantly greater applicability, particularly in the absence of a direct oxygen abundance determination. Nitrogen ICFs and N/O abundances are reported in Table 5.

Despite the very high ionization of J104457 and J141851, we determine smaller N ICFs than the relationships of Peimbert & Costero (1969) and Esteban et al. (2020) for the three-zone model, but find ICFs more similar to Esteban et al. (2020) for the four-zone model. The resulting N/O values are low, but not at odds with the standards of metal-poor galaxies, spanning just 27%–32% and 16%–40% solar for J104457 and J141851, respectively.

Given the very high-ionization emission lines observed from other elements in our spectra, we might expect there to also be emission from high-ionization species of N, but this is also dependent on the abundance of N ions. Unfortunately, the UV N III] emission-line quintuplet around $\lambda 1750$ lies just outside the wavelength coverage of our high-resolution COS spectra, and we only weakly detect the N IV] emission lines at $\lambda\lambda 1483,1487$. However, we can use our optical [N II] $\lambda6584$ and UV N IV] $\lambda\lambda 1483,1487$ line measurements as a guide to compare to expectations from photoionization models.

At the four-zone average ionization parameters characterizing J104457 and J141851, the photoionization models predict relative N^+ , N^{+2} , and N^{+3} ionization fractions of 3.2%, 79.2%, and 17.4%, respectively, for J104457, and 5.4%, 84.4%, and

9.6%, respectively, for J141851. N^{+2} is the clearly dominant species of N in these EELGs. However, at the temperatures and densities measured for J104475 and J141851, the summed emissivity of the two strongest lines of the N III] quintuplet, $\lambda\lambda1749,1752$, is $\sim20\%$ of that of the [N II] $\lambda6584$ line. For the N IV] $\lambda\lambda1483,1486$ lines the emissivity is a bit stronger, at 37%–65% of the [N II] $\lambda6584$ line. Therefore, the weak detections of the N IV] $\lambda\lambda1483,1486$ lines align with the expectations for the low-ionization fraction of N⁺³ and low N abundance of our EELGs.

4.4. C/O Abundances

In a simple three-zone ionization model, C/O can be determined from the C^{+2}/O^{+2} ratio alone, where this assumption is most appropriate for moderate ionization nebulae. For high-ionization nebulae resulting from a hard ionizing spectrum, we must also consider carbon contributions from the C^{+3} species to avoid underestimating the true C/O abundance. However, even if the C IV $\lambda\lambda 1548,1550$ doublet is observed in emission, as is the case with the EELGs studied here, these lines are resonant, and so, determining their intrinsic fluxes and subsequent C^{+3}/H^+ abundances is problematic. Instead, we use the photoionization-model-derived C ICF of Berg et al. (2019b):

$$\frac{\mathrm{C}}{\mathrm{O}} = \frac{\mathrm{C}^{+2}}{\mathrm{O}^{+2}} \times \left[\frac{X(\mathrm{C}^{+2})}{X(\mathrm{O}^{+2})} \right]^{-1} = \frac{\mathrm{C}^{+2}}{\mathrm{O}^{+2}} \times \mathrm{ICF}(\mathrm{C}^{+2}),$$

where $X(C^{+2})$ and $X(O^{+2})$ are the C^{+2} and O^{+2} ionization fractions, respectively.

Carbon ICFs and C/O abundances are reported in Table 5, where the average ionization parameters, $\log U_{\rm ave}$, were used to determine the ICFs for the three- and four-zone models. Note that the C and O abundances presented here have not been corrected for the fraction of atoms embedded in dust. However, the depletion onto dust grains is expected to be small for the low abundances and small extinctions of J104457 and J141851, so the relative dust depletions between C and O should be negligible.

4.5. α-element/O Abundances

Strong collisionally excited emission lines for the α -elements S, Ne, and Ar are observed in the optical LBT/MODS spectra of J104457 and J141851. In particular, we observe significant [S II] $\lambda\lambda6717,6731$, [S III] $\lambda\lambda9069,9532$, [Ar III] $\lambda7135$, [Ar IV] $\lambda\lambda4711,4740$, and [Ne III] $\lambda3869$ emission lines that, with the application of appropriate ICFs, allow us to determine the relative abundances of these elements.

For sulfur abundance determinations in a three-zone nebula, contributions from S⁺, S⁺², and S⁺³ are relevant. Unfortunately, we only observe S emission in the optical spectra from the S⁺ (10.36–22.34 eV) and S⁺² (22.34–34.79 eV) ions that probe the low- to intermediate-ionization zones. Note that while the ionization energy of S⁺ is lower than that of H⁰ (13.59 eV) and [S II] emission may therefore originate from outside the H II region, we showed in Section 4.1 that ionic contributions from the neutral zone are negligible in very high-ionization EELGs. Because there are no strong S⁺³ or S⁺⁴ emission lines in the optical, an ICF is typically required to account for the unseen S species whose ionization energies are concurrent with the O⁺² zone (35.12–54.94 eV).

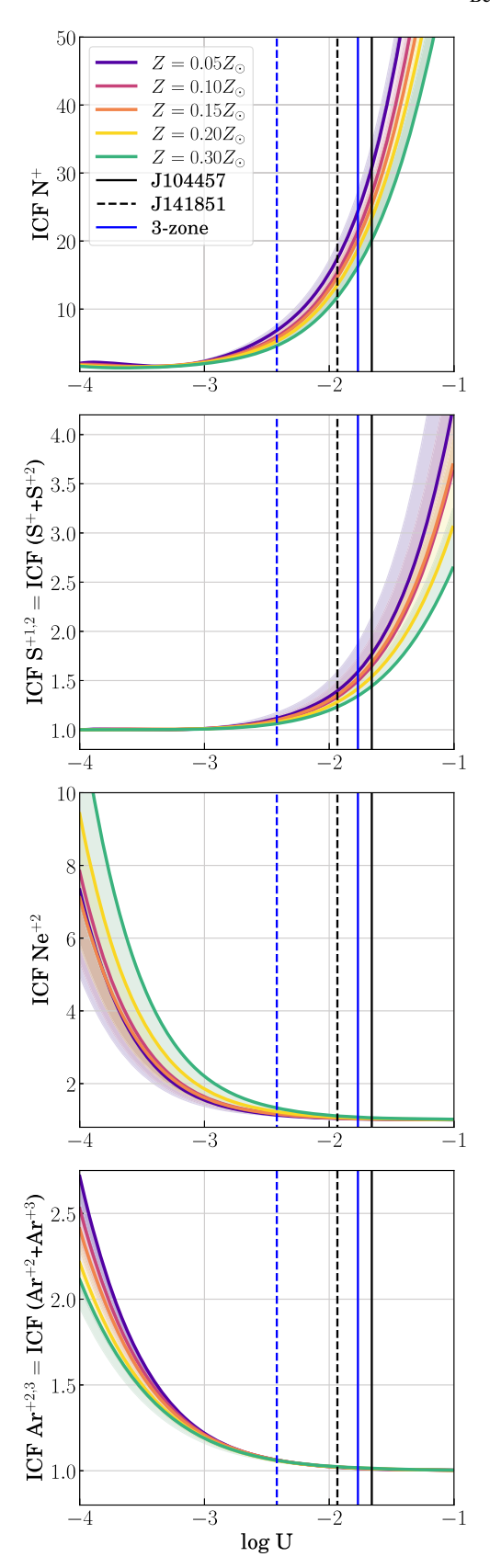


Figure 6. Photoionization models of N, S, Ne, and Ar ionization correction factors versus ionization parameter. Lines are color-coded by the gas-phase oxygen abundance and are centered on models with an age of $t=10^{6.7}$ yr. The light color shading demonstrates that little variation is seen in the ICFs for bursts aging from $t=10^{6.0}$ – $10^{7.0}$ yr. For reference, the log $U_{\rm ave}$ values of J104457 and J141851 are shown for the three-zone (blue) and four-zone (black) models.

Similar to sulfur, two species of Ar are observed, but originating from intermediate- to very high-ionization zones: Ar⁺² and Ar⁺³. While the Ar⁺ volume (15.76–27.63 eV) will also be present within an H II region, its contribution should be very small for the very high ionizations characterizing EELGs. For neon, however, only the high to very high Ne⁺² ionization state (40.96–63.45 eV) is strongly observed in the optical or FUV spectra of EELGs. While this is the dominant ionization zone of these nebulae, we must still correct for possible contributions from other ionization states.

Again, using the photoionization models described in Section 3.1.1, we plot S, Ne, and Ar ICFs as a function of log U in the bottom three panels of Figure 6. For S we see that the ICFs are close to one at low ionization (low $\log U$ values) and steeply increase for log U > -2.5 as the unobserved S⁺³ and S⁺⁴ ionization states become more prominent. On the other hand, the opposite trend is seen for the Ne and Ar ICFs, as the observed high-ionization species come to dominate the nebula for log U > -2.5. As expected, for the average ionization parameter values characterizing the four-zone nebula model of J104457 (solid blue line) and J141851 (dashed blue line), which are significantly greater than -2.5, we measure Ar and Ne ICFs that are consistent with 1.0. For sulfur we measure small, but important ICFs that serve to correct for the weak S IV $\lambda\lambda 1405,1406,1417$ features observed in the FUV spectra of J104457 and J141851.

For reference, we also calculate S and Ar ICFs from Thuan et al. (1995) as

$$\begin{split} & \text{ICF}(\mathbf{S}^{+} + \mathbf{S}^{+2}) = \frac{\mathbf{S}}{\mathbf{S}^{+} + \mathbf{S}^{+2}} \\ &= [0.013 + x\{5.10 + x[-12.78 + x(14.77 - 6.11x)]\}]^{-1}, \\ & \text{and ICF}(\mathbf{Ar}^{+} + \mathbf{Ar}^{+2}) = \frac{\mathbf{Ar}}{\mathbf{Ar}^{+2} + \mathbf{Ar}^{+3}} \\ &= [0.99 + x\{0.091 + x[-1.14 + 0.077x]\}]^{-1}, \end{split}$$

where $x = O^+/(O^+ + O^{+2})$, and Ne ICFs from Peimbert & Costero (1969) as ICF(Ne⁺²) = $(O^+ + O^{+2})/O^{+2}$. For Ar and Ne, where we observe the very high-ionization species directly, the three-zone ICFs adopted from the literature agree within the uncertainties of our results. However, we infer significantly lower S ICFs from our models than from Thuan et al. (1995), resulting in smaller S/O abundances. This difference may be due to significant changes in atomic data for S⁺² over the past few decades (see, e.g., Figure 4 in Berg et al. 2015). All α -element ICFs and abundances are reported in Table 5.

4.6. Fe/O Abundances

While collisionally excited emission lines are commonly observed for one or two species of Fe in H II regions, Fe abundance determinations are often avoided due to the importance of dust depletion, accurate ICFs, and fluorescence. However, several recent studies have revived the interest in Fe abundances by suggesting that enhanced α /Fe abundance ratios are responsible for the extremely hard radiation fields inferred from the stellar continua and emission-line ratios in chemically young, high-redshift galaxies (e.g., Steidel et al. 2018; Shapley et al. 2019; Topping et al. 2020). Given the importance of α /Fe (e.g., O/Fe) abundances to interpreting the ionizing continua of early galaxies, we were motivated to investigate the Fe/O abundances of our EELGs.

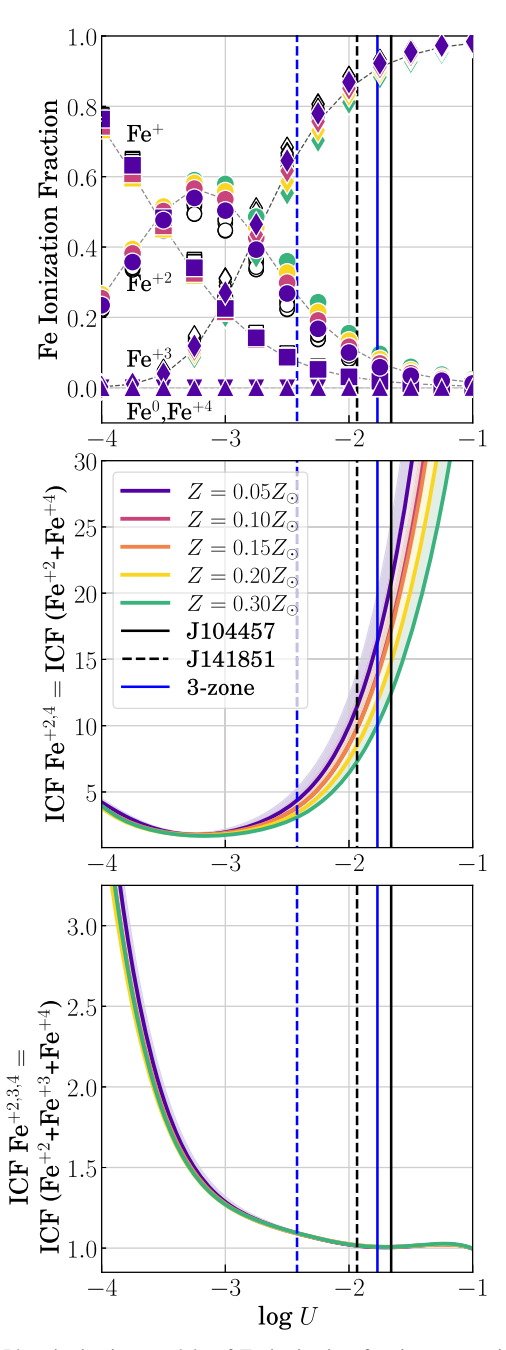


Figure 7. Photoionization models of Fe ionization fraction versus ionization parameter. Top: the changing fractions of Fe species are shown as a function of ionization parameter, where downward-pointing triangles, squares, circles, diamonds, and upward-pointing triangles represent the Fe⁰, Fe⁺, Fe⁺², Fe⁺³, and Fe⁺⁴ ions, respectively. Open symbols designate deviations due to burst age, spanning $t=10^6$ to $t=10^7$ yr. Dashed gray lines trace the $Z=0.1Z_{\odot}$, or $12+\log(O/H)=7.7$, models. Note that the Fe⁰ and Fe⁺⁴ fractions are negligible regardless of ionization parameter. Middle: The model Fe ICF to be used when only Fe⁺² or Fe⁺² + Fe⁺⁴ are observed. Bottom: the model Fe ICF to be used when Fe⁺² + Fe⁺³ or Fe⁺² + Fe⁺³ + Fe⁺⁴ are observed. For reference, the log U_{ave} values of J104457 and J141851 are shown for the threezone (blue) and four-zone (black) models.

In the top panel of Figure 7 we show photoionization models of the ionization fraction of relevant Fe species as a function of ionization parameter. In the standard three-zone ionization model of H II regions, three Fe species are expected to contribute to the abundances: Fe $^+$ in the neutral to low-ionization zone, Fe $^{+2}$ in the low- to intermediate-ionization zone, and Fe $^{+3}$ in the high-ionization zone. For Fe $^+$ we weakly

detected the [Fe II] $\lambda4287.39$, $\lambda5158.79$, $\lambda7637.51$ emission lines. However, most of the [Fe II] lines are significantly affected by fluorescence (Rodríguez 1999). An exception is the [Fe II] $\lambda8617$ emission line, as it is nearly insensitive to the effects of UV pumping (Rodríguez 2003), but this line was not detected in J104457 or J141851. Fortunately, the Fe⁺ ion has an ionization potential that mostly spans the neutral zone (7.902–16.188 eV). We therefore forego an Fe⁺ abundance determination.

Fe⁺² is the species of Fe that is most commonly used for abundance determinations in H II regions. In the LBT/MODS spectra, we detect [Fe III] $\lambda 4658.50$, $\lambda 4701.53$, $\lambda 4880.99$, and $\lambda 5270.40$. Of these lines, both [Fe III] $\lambda 4659$ is the strongest (by a factor of 2–4). We determine Fe⁺²/H⁺ abundances from the $\lambda 5270$ line that are larger by a factor of 2 than those determined by the $\lambda 4659$. Given the wide usage of the [Fe III] $\lambda 4659$ line in Fe abundance determinations, and its dominance of the Fe lines in our spectra, we therefore use the [Fe III] $\lambda 4659$ alone to determine Fe⁺²/H⁺ abundances.

In the proposed four-zone model, Fe⁺³ bridges the intermediate- and high-ionization zones, while Fe⁺⁴ is a *pure* very high-ionization ion. Fe⁺³ is often undetected owing to its relatively weak emissivities. In fact, for the high electron temperatures of our targets, the emissivities of [Fe IV] λ 4907 and λ 5234 are only 6.3% and 2.5%, respectively, relative to the [Fe III] λ 4659 line. Thus we only weakly detect [Fe IV] λ 4906.56 in J104457 and [Fe IV] λ 5233.76 in J141851, but are able to use these lines to estimate Fe⁺³/H⁺ abundances.

For Fe⁺⁴, we detect emission from [Fe V] λ 4143.15 and λ 4227.19 in the optical LBT/MODS spectra of J104457 and J141851. However, this is not terribly surprising given the very high ionization of our EELGs and the strong emissivities of these lines at high electron temperatures ($j_{\lambda 4143}/j_{\lambda 4659} = 0.27$ and $j_{\lambda 4227}/j_{\lambda 4659} = 1.39$). While [Fe V] λ 4227 is rare, it has also been reported for other EELGs, such as SBS 0335-052 (Izotov et al. 2009).

Considering the Fe emission lines observed in the optical spectra of J104457 and J141851, we calculate Fe/H abundances four different ways:

$$\begin{split} &1.\,\frac{Fe}{H} = \frac{Fe^{+2}}{H^+} \times ICF(Fe^{+2}),\\ &2.\,\frac{Fe}{H} = \frac{Fe^{+2}}{H^+} \times ICF(Fe^{+2}) \, (I09),\\ &3.\,\frac{Fe}{H} = \frac{Fe^{+2} + Fe^{+4}}{H^+} \times ICF(Fe^{+2,4}), \, \text{and}\\ &4.\,\frac{Fe}{H} = \frac{Fe^{+2} + Fe^{+3} + Fe^{+4}}{H^+} \times ICF(Fe^{+2,3,4}). \end{split}$$

The first two equations follow the common method of determining Fe/H from Fe⁺², where the ICF is the Fe⁺² ionization fraction, $X(\text{Fe}^{+2})$, from our photoionization models for Equation (1) and is from Izotov et al. (2009) for Equation (2). The third method incorporates our [Fe V] λ 4227 observations such that the ICF must only correct for Fe⁺ and Fe⁺³, as in the middle panel of Figure 7. Fourth, we used all of the observed Fe species in our optical spectra with the ICF from the bottom panel of Figure 7, where ICF(Fe^{+2,3,4}) = ICF(Fe⁺²+Fe⁺³+Fe⁺⁴) = $X(\text{Fe}^{+2}) + X(\text{Fe}^{+3}) + X(\text{Fe}^{+4})$. Finally, we used

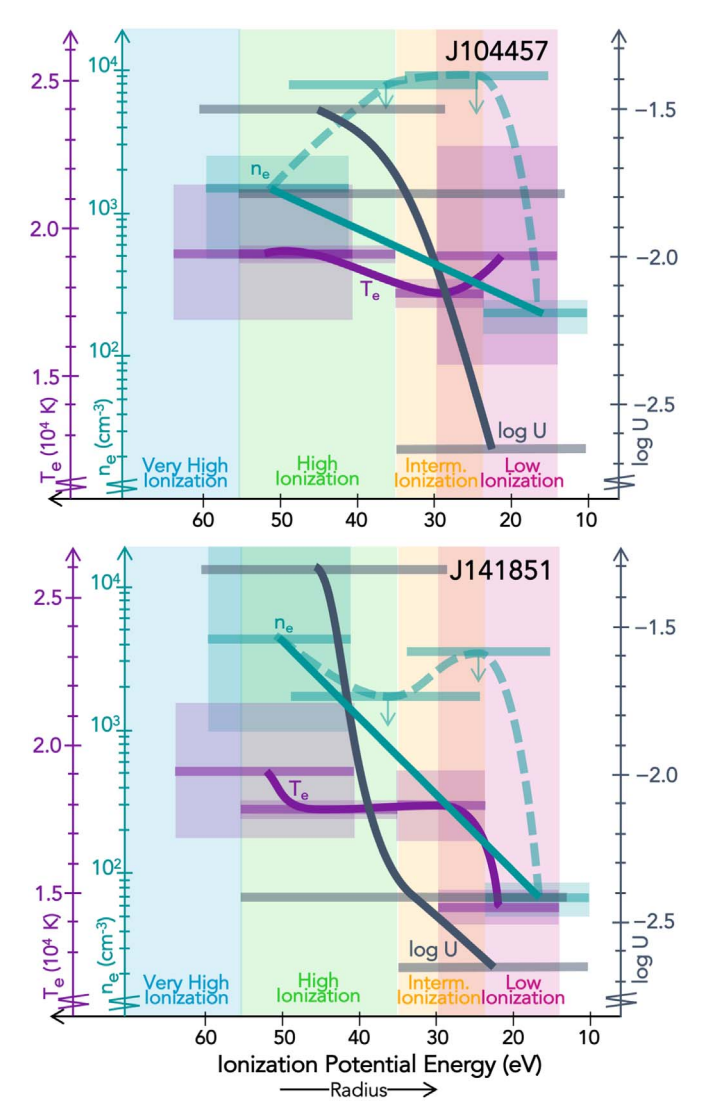


Figure 8. A toy model view of the structure of a spherical EELG H II region. We used the electron temperature (purple), electron density (green), and ionization parameter (gray) measurements for multiple ionization zones to trace their changing nature as a function of radius for J104457 (top) and J141851 (bottom). Each measurement is plotted as a horizontal bar extending the length of its corresponding ion's ionization potential energy and, for T_e and n_e , with a shaded vertical box representing the uncertainty. Note that two density structures are traced for each galaxy: (1) the darker green line connects the two density measurements made from the optical spectra that characterize the very high-and the low-ionization zones and (2) the lighter green line connects all four density measurements, including the upper limits for the high- and intermediate-ionization zones derived from the UV spectra.

the four methods of Fe/H abundance determinations to derive relative Fe/O, or Fe/ α , as reported in Table 5.

5. Insights Into Physical Properties of EELGs

In this work we have explored the physical properties of two EELGs for both the classical three-zone ionization model and the proposed four-zone ionization model. In Sections 3.1.1 and 3.2.2 we showed that examining multiple optical elemental line ratios allows us to probe the sub-volumes that compose a nebula in terms of their the temperature, density, and ionization structures. We map out these measurements in Figure 8. If we visualize our H II regions with our simplified concentric shells

model, then we can overplot the general shapes of how temperature, density, and ionization change as a function of radius.

Altogether, the multiple temperature, density, and ionization measurements used in this work provide a unique picture of the physical properties in EELGs. Specifically, the ionization parameter measurements inform us of the basic shape of the ionizing radiation field and subsequent ionization structure. For J104457 and J141841, the line ratios are indicative of a steep ionization gradient that is more highly ionized in the center and decreases with radius. The resulting ionization parameters measure an extreme change in the density of high-energy ionizing photons across these nebulae, suggesting that most of the high-energy ionizing photons are absorbed in the inner high- and very high-ionization volumes.

This new physical model of EELGs has important implications for the understanding and interpretation of both local EELGs and their high-redshift counterparts that are likely important drivers of reionization. Perhaps most importantly, the ionization parameters in EELGs are misrepresented by the standard three-zone model, indicating that harder radiation fields are present in these galaxies than previously thought. Here we discuss further differences between the two models and their implications for interpreting EELGs in both the nearby and early universe.

5.1. Implications for Abundance Determinations

5.1.1. CNO Abundances

The oxygen abundance of a galaxy is an important quantity, used to characterize its chemical and evolutionary maturity. Reassuringly, even for the high-energy ionizing radiation fields present in EELGs, the fraction of total O ions that are in a very high-ionization state (e.g., O^{+3}) is very small, and so the measured O/H abundance is essentially unaffected by the choice of a three- versus four-zone model. Interestingly, while the $O^{+3}/O_{\text{tot.}}$ fractions indicate that only 1%–2% of the oxygen ions are in the O^{+3} state, the elevated log U_{high} and n_e values determined for the high- to very high-ionization volume in Section 3.2 suggests that a significant fraction of the ionizing photons are absorbed by the very high-ionization volume.

Arguably the next most useful abundance for characterizing galaxies is the relative N/O abundance. The observed scaling of nitrogen with oxygen has long been understood as a combination of primary (metallicity-independent) nitrogen production plus a linearly increasing fraction of secondary (metallicity-dependent) nitrogen that comes to dominate the total N/O relationship at intermediate metallicities (e.g., Costas & Edmunds 1993; van Zee & Haynes 2006; Berg et al. 2012). Owing to this important trend, ratios of the strength of N emission relative to O emission and H α emission are popular strong-line metallicity diagnostics, especially the [N II] λ 6584/ $H\alpha \lambda 6563$ diagnostic for studies of moderate redshift galaxies. However, because oxygen is primarily produced by massive stars on relatively short timescales (\$\leq 40\text{ Myr}\right), while nitrogen is produced by both massive and intermediate mass stars on longer times scales ($\sim 100 \,\mathrm{Myr}$), the N/O ratio is sensitive to the past star formation efficiency of a galaxy and serves as a

clock since its most recent burst (e.g., Henry et al. 2000; Berg et al. 2020). Therefore, while N/O variations may pose a challenge to simple strong-line calibrations, they also serve as a powerful tool when considered as part of the abundance profile of a galaxy. In this context, the very low N/O values measured for J104457 and J141851 may indicate that the most recent burst of star formation is very young.

The total C/O abundances determined in Section 4.4 rely on the emission ratio from C^{+2} and O^{+2} ions, which benefit from having similar excitation potentials and overlapping ionization ranges, and so should not be significantly affected by non-uniform density and temperature distributions in the nebulae. As expected, both J104457 and J141851 have C/O abundances of roughly $30\%~(C/O)_{\odot}$ that vary by less than 10% between the three-zone and four-zone ionization models.

In contrast to C/O abundances, ionic C abundances show large differences between the three-zone and four-zone ionization models. Using our detailed nebular analysis of J104457 and J141851 as constraints, we can use CLOUDY models to predict the intrinsic C IV $\lambda\lambda1548,1550$ flux produced by photoionization. For example, assuming reasonable values for our EELGs: $Z_{\rm neb} = [0.05,0.10]\,Z_{\odot}$, $C/O_{\rm neb} = 0.25$ (C/O) $_{\odot}$, log U = -1.5, a stellar population age of [10^{6.5}, 10^{6.7}] yr, and uniform density of $n_e = [10^2,\ 10^3]\,{\rm cm}^{-3}$, the predicted C IV $\lambda\lambda1548,1550/C\,{\rm III}]\,\lambda\lambda1907,1909$ ratio is 0.40–0.72. These flux ratios correspond to model C^{+3}/C^{+2} ratios of 0.23–0.43.

In comparison, the observed C IV $\lambda\lambda1548,1550/C$ III] $\lambda\lambda1907,1909$ ratio is [0.91, 0.26], corresponding to C⁺³/C⁺² ratios of [0.22, 0.07] for [J104457, J141851]. These values suggest that J104457 produces C IV emission in close agreement of what current models predict, while only ~20%, at most, of the predicted C IV emission produced by J141851 is escaping the galaxy (see Berg et al. 2019a).

As shown in this work, interpreting the physical properties of EELGs is complicated. The relative emission from different ions is affected by many parameters, and, thus, accurate abundance measurements require a detailed understanding of the physical conditions of the nebulae. Ionic abundance determinations for ions spanning different ionization zones are particularly sensitive to the temperature distribution (see Appendix). Interestingly, density also plays a large role in our interpretation of C IV]. The true density distributions of our nebulae are likely complex, clumpy structures, but our simplified four-zone model in which C III] emission originates primarily from the intermediateionization zone and C IV emission from the very high-ionization zone provides an informative upper limit. If we employ the full range of densities that we measure such that CIII] emission is associated with $n_e = (320, 130) \text{ cm}^{-3}$ gas and C IV emission is associated with $n_e = (1550, 2110) \text{ cm}^{-3} \text{ gas for J} 104457,$ J141851, respectively, then the photoionization models can reach remarkably large C IV $\lambda\lambda 1548,50/C$ III] $\lambda\lambda 1907,09$ ratios of [8.54, 5.18] for [0.05,0.10] Z_{\odot} . While the intrinsic flux of the C IV $\lambda\lambda 1548,1550$ resonant doublet can theoretically be used to estimate the escape of C IV emission as a proxy for the escape of high-energy photons through high-ionization gas (Berg et al. 2019a), the models are currently too unconstrained to be useful.

5.1.2. \(\alpha \) Abundances

Neon: for Ne/O abundances, we observe strong [Ne III] emission, which originates partially from the very high-ionization zone and partially from the dominant high-ionization zone. Therefore, the Ne ICFs from both our models and

¹³ The shape of the ionizing radiation field and the resulting nebular emission lines are also significantly affected by dust. However, this is not likely a concern for the EELGs studied here, which have well-determined, very low reddening values.

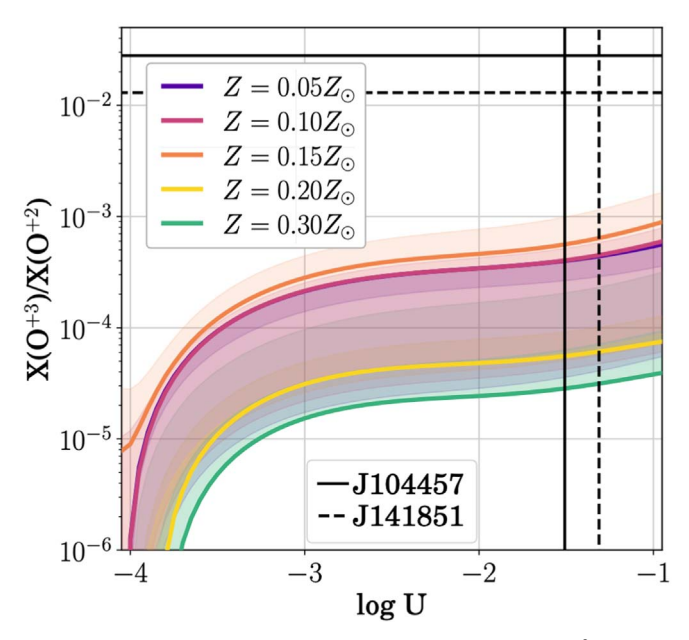


Figure 9. Photoionization models of the ionization fraction of O^{+3} relative to O^{+2} versus ionization parameter. Models of a given metallicity (indicated by color) are shown for a burst age of $10^{6.7}$ yr (solid line) and spanning 10^6-10^7 yr (shaded regions). Even for the low metallicities and high log $U_{\rm high}$ values (vertical lines) measured for J104457 and J141851, the models fail to reproduce the O^{+3} fraction determined from the UV O IV emission lines (horizontal lines).

Peimbert & Costero (1969) are close to unity, implying small corrections and uncertainties. As shown in Table 5, the Ne/O abundances for both cases are approximately solar for J104457 and the three-zone model of J141851, but subsolar for the four-zone model. At the higher temperatures used in the four-zone model, there must be a smaller fraction of Ne⁺² ions to produce the observed emission lines (see Figure 14 in Appendix), resulting in lower abundances. Interestingly, the fact that Ne/O abundances of the three-zone model agree more closely with the expected solar ratio may indicate that very little of the [Ne III] λ 3869 emission originates from the very high-ionization zone. Because the high-ionization zone dominates our nebulae (O⁺²) and Ne + 2 is a bridge ion, this is not terribly surprising.

Argon: for Ar/O abundances, we observe strong [Ar III] and [Ar IV] emission, spanning, in part, the dominant high-ionization zone and beyond. Therefore, similar to Ne, the Ar ICFs are close to unity for both our models and those of Thuan et al. (1995), who also utilized [Ar IV] emission when present. The Ar/O abundances we derive are approximately equal to or greater than solar for the three-zone model, but are slightly subsolar for the four-zone model, regardless of our choice of ICF.

Sulfur: for S/O, we measure strong emission lines from [S II] and [S III], spanning the low- and intermediate-ionization zones, but no strong features probing the dominate high-ionization zone. Therefore, to determine S/O ICFs, we created models specifically tailored to the conditions of EELGs. Adopting these new ICFs (see Figure 6 and the four-zone ionization model, we find S/O abundances that are roughly $[62\%, 51\%](S/O)_{\odot}$.

As a test of our ICFs, we can use our weakly observed S IV λ 1406 fluxes to estimate the S⁺³/S⁺² ratio. Using a combination of line ratios from both our UV and optical

spectra, we determine $S^{+3}/S^{+2} = (S^{+3}/O^{+2})_{UV}/(S^{+2}/O^{+2})_{opt.}$ values of [1.36,0.44] for [J104457, J141851] using the fourzone model. In comparison, these S^{+3}/S^{+2} fractions are significantly higher than those predicted by our photoionization models: [0.60, 0.77] for the [three-zone, four-zone] model in J104457 and [0.11, 0.38] for the [three-zone, four-zone] model in J141851.

Correcting for the estimated S^{+3} contributions would require additional ICFs of [1.77, 1.16] and result in higher S/O abundances of [110%, $60\%](S/O)_{\odot}$. We see large variations between the three-zone and four-zone models and variations between the model ICFs and using the UV line fluxes of up to 80%. These large uncertainties associated with sulfur abundances in our EELGs are due to the lack of secure measurements of ions from the dominant high-ionization zones. However, the S/O abundances of our EELGs seem to be subsolar regardless of the model used.

5.2. The High-energy Ionizing Photon Production Problem

In the very high-ionization nebulae of EELGs, proper ICFs are especially important to account for the potentially significant unseen ionization states. We can test the robustness of our ICFs by comparing our observations of *pure* very high-ionization species, such as O^{+3} and Fe^{+4} , to their model predictions. In Figure 9 we consider the O^{+3}/O^{+2} ratio, comparing our photoionization models (colored lines) with the measured ratios from the UV spectra of J104457 and J141851. Similar to the long-standing problem of nebular He II production in blue compact dwarf galaxies (e.g., Kehrig et al. 2015, 2018; Berg et al. 2018; Senchyna et al. 2019; Stanway & Eldridge 2019), we are clearly unable to reproduce O^{+3} ionizing flux with stellar populations alone. Even for the extreme conditions in J104457 and J141851 and the small O⁺³ contribution fractions measured for them, the photoionization models under-predict the O^{+3}/O^{+2} ratio by more than an order of magnitude. Additionally, we detect emission from [Fe V] $\lambda 4143.15$ and $\lambda 4227.19$ in the optical LBT/MODS spectra of J104457 and J141851, and yet, the model Fe⁺⁴ ion fraction in Figure 7 is negligible even for very high-ionization parameters. 14 This discrepancy is indicative of the failure of photoionization models to accurately represent the conditions producing the very high-ionization zone in EELGs. Specifically, there seems to be a high-energy ionizing photon production problem (HEIP³) that current stellar population synthesis models alone cannot solve.

The HEIP³ has little effect on our resulting oxygen abundance measurements (see Table 5) because we observed emission from the dominant ion in the nebula, O⁺². Similarly, for Ne and Ar we measure the species covering the dominant high-ionization zone, and so our modeled ICFs, and subsequent abundance determinations, have small uncertainties. On the other hand, the HEIP³ may significantly affect our interpretation of elements with only low-ionization species observed, such as S and N. For S we observe S⁺ and S⁺², but both become trace ions in very high-ionization nebulae such that they require large, robust ICFs to determine accurate S/H abundances. The case for N/H abundances is similar. Therefore, our N/H, S/H, and S/O abundances are likely biased

 $[\]overline{{}^{14}}$ Note that the ICF(Fe⁺²) in the middle panel of Figure 7 is equivalent to ICF(Fe⁺²+ Fe⁺⁴) = X(Fe⁺²)+X(Fe⁺⁴) because the X(Fe⁺⁴) contribution is erroneously negligible in the models. Thus, ICF₁ = ICF₃ in Table 5.

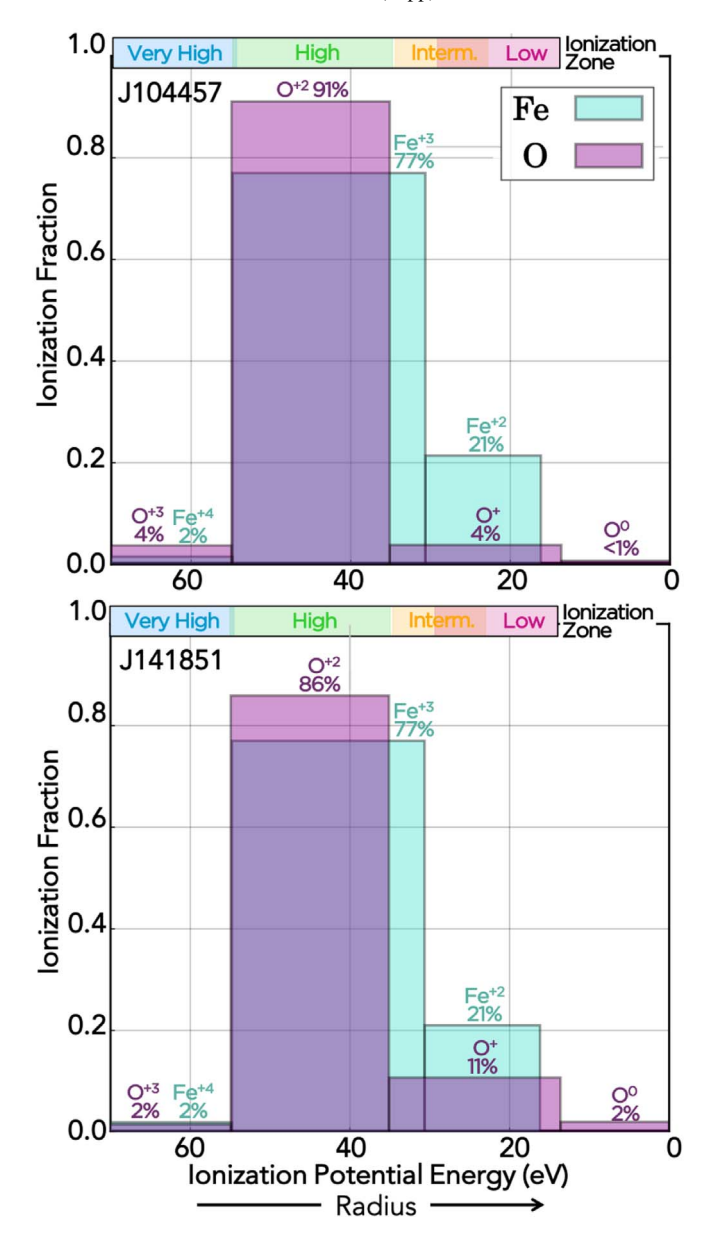


Figure 10. Ionization structure of two EELGs based on the O and Fe ionic abundance fractions reported in Table 5. The O and Fe ions trace slightly different ionization potential ranges, yet for both EELGs, the nebular ionization structure is similar. While the high-ionization zone clearly dominates the ionic abundances for both EELGs, the very high-ionization ions are still important for interpreting the volume-averaged ionization parameter.

low. Relative N/O abundances may be an exception, as the N^+ and O^+ ions used in the calculation trace each other fairly closely, and so should require similar ICFs. However, the values in Table 5 suggest that N/O determinations are in fact rather sensitive to different ICFs in the extreme environments of EELGs.

In general, for our EELGs, the HEIP³ results in underestimated ionization parameters and ICFs that underestimate total abundances for observations of low-ionization species, but has negligible effect when bridge and pure very high-ionization species are observed. These biases may be even more extreme at high redshifts, where conditions are expected to be more extreme. Iron, however, presents an interesting exception to this rule due to the so-called [Fe IV] discrepancy: ICFs derived from photoionization models overpredict Fe⁺³ abundances by

more than a factor of four compared to observations (Rodríguez & Rubin 2005, and references therein). Similarly, we find our ICFs to predict a larger contribution from Fe $^{+3}$ than we measure directly from [Fe IV], by a factor of $\sim\!2\text{--}5$. Given these Fe $^{+3}$ and Fe $^{+4}$ discrepancies, further high S/N observations are needed to empirically constrain the Fe $^{+3}$ and Fe $^{+4}$ contributions to the Fe ICF.

5.3. The Abundance Profile of EELGs: Evidence of Hard Radiation Fields?

We examined ionic abundances of O, N, C, Ne, Ar, S, and Fe in the previous sections to better understand the ionic structure of EELGs. Figure 10 summarizes our resulting ionization model using the ionic abundances measured for O and Fe, which allow us to map each of the zones in the fourzone ionization model. For both J104457 and J141851, the high-ionization ions clearly dominate their respective elements such that the very high-ionization zone has little effect on the total abundance. However, the very high-ionization zones do play an important role in our interpretation of the volume-averaged ionization parameter of a galaxy.

In general, we found that (1) photoionization models with stellar-population SEDs generally fail to reproduce the high-ionization species observed in EELGs (the HEIP³), (2) the higher ionization parameters determined for the four-zone model indicate a larger fraction of metals are in high-ionization states than predicted in the three-zone model, and (3) the higher temperatures assumed in the four-zone model can reduce abundances of high-ionization species. The latter point means that if high temperatures play a critical role in EELGs, then nebular abundances determined primarily from their high-ionization lines may be somewhat overestimated by the standard three-zone model. On the other hand, point (2) results in elemental abundances determined primarily from their lower-ionization species (i.e., N, S, and Fe) being underestimated by the three-zone model.

Regardless of the ionization model, we measured all elements to be significantly subsolar for J104457 and J141851, as expected for low-mass galaxies. However, the various elements span a range of abundances relative to solar from 1.9%-5.8% for J104457 and 2.6%-8.7% for J141851, using the four-zone model. To better compare the abundance profiles for J104457 and J141851, as determined by the threeand four-zone models, we report the adopted elemental abundances relative to solar in Table 6. In general, we have adopted the abundances determined with the ICFs of this work. Given the sensitivity of the S/H calculations to the assumed ICF and, subsequently, the large uncertainties, we do not analyze the S/H abundances further. For Fe, we consider the opposing challenges of the photoionization models for different Fe ions, and thus adopt the log(Fe/O) abundances based solely on the Fe⁺ measurements for the three-zone model and the log (Fe/O) based on Fe⁺ + Fe⁺³ abundances for the four-zone

We find that the abundances in Table 6 naturally split into two populations: (1) α -elements: Ar/H, and Ne/H, which have abundances relative to solar consistent with O/H, and (2) non- α -elements: N/H, C/H, and Fe/H, which have solar-scaled abundances that are deficient relative to O/H and the other α -elements. The α -element trend aligns with typical nucelosynthetic arguments, where O, S, Ar, and Ne are all produced predominantly on short timescales (\leq 40 Myr) by core-collapse

Table 6Abundance Profiles of Two EELGs

	J104457	
Solar Fraction	3 Zone 4 Zone	3 Zone 4 Zone
	α -Elements:	
$(O/H)/(O/H)_{\odot}$	$0.056 \pm 0.002 \mid 0.058 \pm 0.003$	$0.084 \pm 0.003 \mid 0.087 \pm 0.003$
$(Ar/H)/(Ar/H)_{\odot}$	$0.052 \pm 0.008 \mid \ 0.051 \pm 0.008$	$0.104 \pm 0.012 \mid \ 0.077 \pm 0.013$
$(Ne/H)/(Ne/H)_{\odot}$	$0.053 \pm 0.011 \mid \ 0.053 \pm 0.018$	$0.085 \pm 0.012 \mid \ 0.054 \pm 0.014$
	Non α -Elements:	
$(N/H)/(N/H)_{\odot}$	$0.015 \pm 0.004 0.019 \pm 0.002$	$0.013 \pm 0.002 \mid 0.035 \pm 0.006$
$(C/H)/(C/H)_{\odot}$	$0.018 \pm 0.004 0.020 \pm 0.006$	$0.022 \pm 0.006 0.027 \pm 0.006$
$(Fe/H)/(Fe/H)_{\odot}$	$0.015 \pm 0.004 \mid 0.020 \pm 0.003$	$0.009 \pm 0.002 \mid 0.026 \pm 0.003$

Note. Total abundances of J104457 and J141851 relative to solar. The abundances are split into two groups of similar chemical composition. For N, Ar, Ne, and Fe, where we reported we reported multiple abundances derived from different ICFs, we have adopted the abundances using ICFs derived in this work. For Fe, we use ICF(Fe⁺²)² for the three-zone model and ICF(Fe⁺²+ Fe⁺⁴)³ for the four-zone model.

supernovae (SNe), and so should all follow a consistent abundance profile. However, the recent chemical evolution models of Kobayashi et al. (2020) indicate that while oxygen is produced mostly by CC SNe and a bit by AGB stars, S and Ar also have a significant contribution from Type Ia SNe (29% and 34% respectively), resulting in delayed enrichment relative to the CC SNe production. In this case, the variations in abundances ranging roughly 5%–6% Z_{\odot} and 5%–9% Z_{\odot} in the α -elements for J104457 and J141851, respectively, may be explained by the individual star formation histories of these galaxies.

In contrast, the solar-scaled non- α -element abundances are roughly 2–3 times lower than those of the α elements. One concern is that Fe strongly depletes onto dust and so the Fe abundances may be strongly affected such that Fe/H is biased to even lower abundances. Izotov et al. (2006) measured subsolar Fe/O abundance ratios from metal-poor galaxies in the Sloan Digital Sky Survey DR3, suggesting that iron depleting onto dust grains was responsible, but that this effect decreases with decreasing metallicity. Therefore, the effect should be small for the low metallicities and very small reddening values of our EELGs. Further, Table 6 shows that Fe and N have similar abundance levels relative to solar, but N does not deplete onto dust, so the level of Fe dust depletion is likely to be small. If high dust destruction rates are occurring in these metal-poor galaxies due to their very hard radiation fields, then Fe may not be significantly locked up in dust. But even if we are missing a fraction of the Fe abundance, the N/H and C/ H abundances suggest that the α elements are truly underabundant, perhaps due to the longer timescales of their production via Type Ia SNe and AGB stars.

5.3.1. \(\sqrt{Fe Enrichment} \)

This result of enhanced $\alpha/{\rm Fe}$ abundances has been suggested as the source of the extremely hard radiation fields inferred from the stellar continua and emission-line ratios in chemically young, high-redshift galaxies (e.g., Steidel et al. 2018; Shapley et al. 2019; Topping et al. 2020). These authors argue that the highly super-solar O/Fe abundances ($\sim 4-5 \times ({\rm O/Fe})_{\odot}$) are expected for the brief star formation histories of $z\sim 2-3$ galaxies, whose enrichment is dominated by the corecollapse SNe products of their recent burst of star formation. In this case, O dominates the cooling and emission lines of the ionized gas, whereas Fe determines FUV opacity and mass-loss rate from massive stars (although this effect is less certain in

very metal-poor stars), resulting in a harder extreme UV radiation field than would be generated by stars and gas with a solar O/Fe composition.

BCDs have also been argued to be cosmologically young systems that formed most of their stellar mass in the past \sim 2 Gyr (e.g., Guseva et al. 2001; Pustilnik et al. 2004; Papaderos et al. 2008). However, Papaderos et al. (2008) found the SDSS imaging morphologies of a sample of BCDs, including J104457, to reveal a redder stellar host implying these galaxies are unlikely to be forming their first generation of stars. Further, Janowiecki et al. (2017) found that the spectral energy distributions of BCDs in the Local Volume Legacy survey (LVL; Dale et al. 2009) were better fit with a two-burst model than a single-burst, with old stellar populations ranging from \sim 3–5 Gyr in age. Therefore, Fe-poor massive stars are not expected to be prevalent in local BCD galaxies due to their longer, complicated star formation histories that result in Fe enrichment from older stars.

For J104457 and J141851, we measure O/Fe abundances that are similar to the values inferred from $z \sim 2-3$ galaxies $(\gtrsim 3 \times (O/Fe)_{\odot})$, but seem to have a different origin. Due to the different timescales of CC SNe and Type Ia SNe, young bursts of star formation in EELGs may result in increased O/Fe ratios due to a recent injection of O, where the associated Fe has not yet been released by Type Ia SNe. This idea is supported by the chemical evolution models of Weinberg et al. (2017), where a sudden burst of star formation with an initial abundance of $Z = 0.3Z_{\odot}$ can temporarily boost O/Fe by up to \sim 0.45 dex if a significant fraction of the gas is consumed and the core-collapse SNe yields are retained. The effect is expected to be even stronger for the very low metallicities of our EELGs, and could then account for the α /Fe enhancement observed. However, this model is complicated by the expectations for low-mass galaxies to have high metal-loading factors (Peeples & Shankar 2011; Chisholm et al. 2018) and a range of effective oxygen yields (Yin et al. 2011; Berg et al. 2019b).

We explore the potential impact of α/Fe enrichment on the observed emission-line ratios of EELGs in Figure 11. To do so, we compared two CLOUDY photoionization models with gasphase parameters matched to our EELGs and an input BPASS ionizing SED with a metallicity either matched to the gas phase $(Z=0.05Z_{\odot})$ or 10 times deficient relative to the gas phase $(Z=0.005Z_{\odot})$. The latter case mimics extreme α/Fe enrichment. The resulting percent differences in the emission-line fluxes are plotted in Figure 11 as a function of radius. The

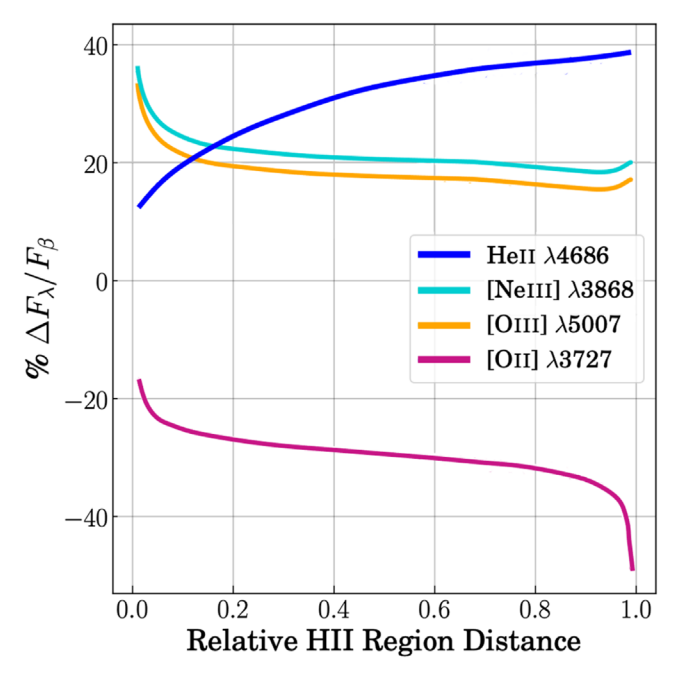


Figure 11. Fractional difference in emission-line fluxes for an α/Fe -enriched photoionization model (i.e., gas abundance > stellar abundance) relative to a classic model (i.e., gas abundance = stellar abundance) for metal-poor $(Z=0.05Z_{\odot})$ EELGs with log U=-1 and a BPASS ionizing SED with a burst age of $t=10^{6.5}$ yr. In general, α/Fe enhancement results in low-ionization emission such as [O II] $\lambda 3727$ decreasing and high-ionization emission like [O III] $\lambda 5007$ and [Ne III] $\lambda 3868$ increasing. Interestingly, very high-ionization emission like He II $\lambda 4686$ becomes more radially extended as a result of α/Fe enrichment.

 $\alpha/{\rm Fe}\text{-enriched}$ model produces larger flux ratios for high-ionization emission lines, by up to ${\sim}40\%$ for lines such as He II $\lambda4686,~{\rm [O~III]}~\lambda5007,~{\rm and}~{\rm [Ne~III]}~\lambda3868,~{\rm and}~{\rm smaller}~{\rm flux}$ ratios for low-ionization lines such as ${\rm [O~II]}~\lambda3727.$ However, even the boosted He II fluxes of this extreme $\alpha/{\rm Fe}\text{-enriched}$ model fail to reproduce the observed He II/H β ratios of EELGs (0.01–0.02) by a factor of 5–10. Therefore, $\alpha/{\rm Fe}$ enrichment may be responsible for the observed properties of typical $z\sim2\text{--3}$ galaxies, such as the BPT offset to higher [O~III]/H β values (e.g., Strom et al. 2017), but it catastrophically fails to solve the HEIP³ in EELGs.

5.4. The Ionization Structure of EELG Nebulae

In Section 3.2.2, we calculated three different volume-averaged ionization parameters to characterize different ionization zones: $\log U_{\rm low}({\rm [S~III]/[S~II]})$, $\log U_{\rm int}({\rm [O~III]/[O~II]})$, and $\log U_{\rm high}({\rm [Ar~IV]/[Ar~III]})$. Together, these three $\log U$ estimates describe an ionization structure gradient that is more highly ionized in the center and decreases with radius.

We demonstrate the theoretical ionization structures of photoionized nebulae in the top left panel of Figure 12. Here we compare three CLOUDY photoionization models with parameters matched to our EELGs, but different ionizing radiation field strengths, as defined by the initial ionization parameter, log U_{init} at the illuminated face of the cloud. Keeping all other parameters identical, the only differing variable between the gray, turquoise, and gold models is the flux density of ionizing photons as a function of radius. The pink model is the same log $U_{init} = -1 \alpha/\text{Fe-enriched model}$ as plotted in Figure 11. The flux density of ionizing photons as a function of radius was output using the SAVE IONIZING

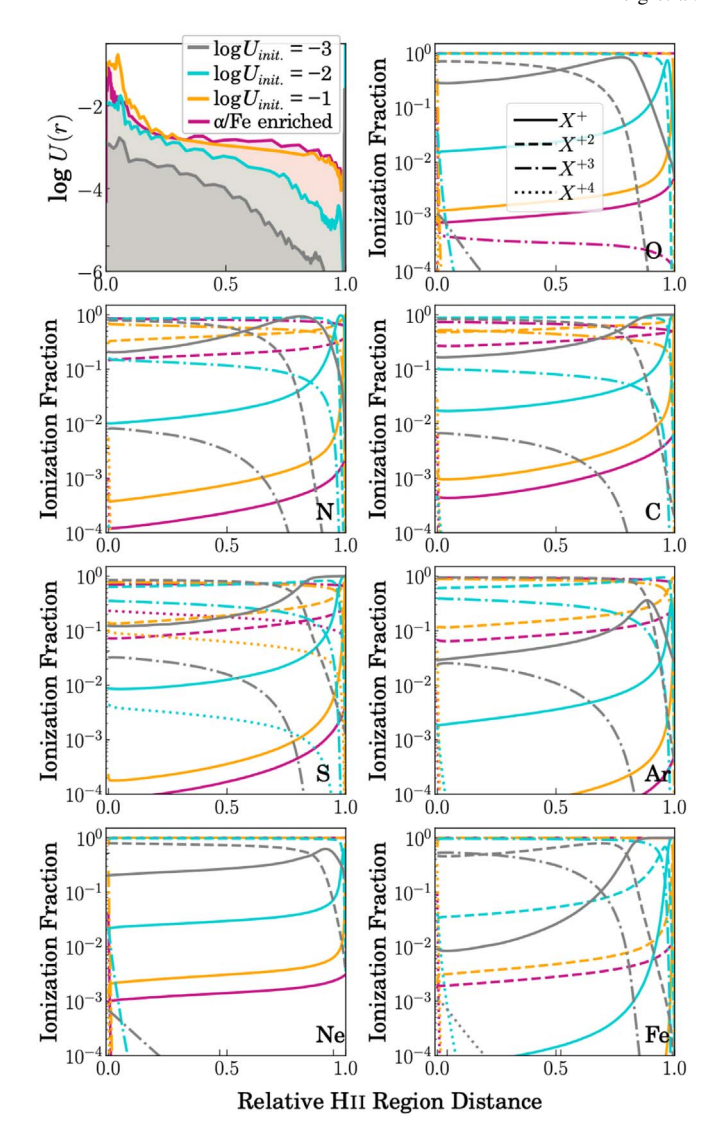


Figure 12. Photoionization models showing how the ionization structure of a simple sphere changes as a function of radius within an H II region for different ionization parameters, as defined at the initial face of the cloud. Specifically, the top left panel shows the ionization parameter gradient and the other panels compare how the ionization fraction profiles of a given element compare.

CONTINUUM command with the EVERY keyword. This combination prints the number of ionizing photons within a given frequency bin for each radial zone (cm⁻² s⁻¹), defined here as $\Phi = Q/(4\pi \cdot r^2)$. Then the ionization parameter in a zone at radius r, U(r), is just $\Phi(r)/n_H/c$, where n_H is the hydrogen density and c is the speed of light. We use the log $U_{\rm init} = -1$ and $\log U_{\rm init} = -2$ models as a good approximation for the large $\log U_{\rm high}$ values determined for the very highionization zones of our EELGs and use the log $U_{\rm init} = -3$ model to represent typical H II regions (e.g., Dopita et al. 2000; Moustakas et al. 2010). In comparison, the inner ionization structure of EELGs is steeper than is expected for typical HII regions by a factor of 10. This extreme ionization structure is also demonstrated by the large $\Delta \log U$ values (-1.14, -1.35) observed across the different ionization volumes of our EELGs, suggesting that most of the high-energy ionizing photons are absorbed in the inner high- and very high-ionization volumes.

While we have shown that this type of detailed analysis is very useful for interpreting the physical properties of nearby galaxies, it does not directly translate to practical applications

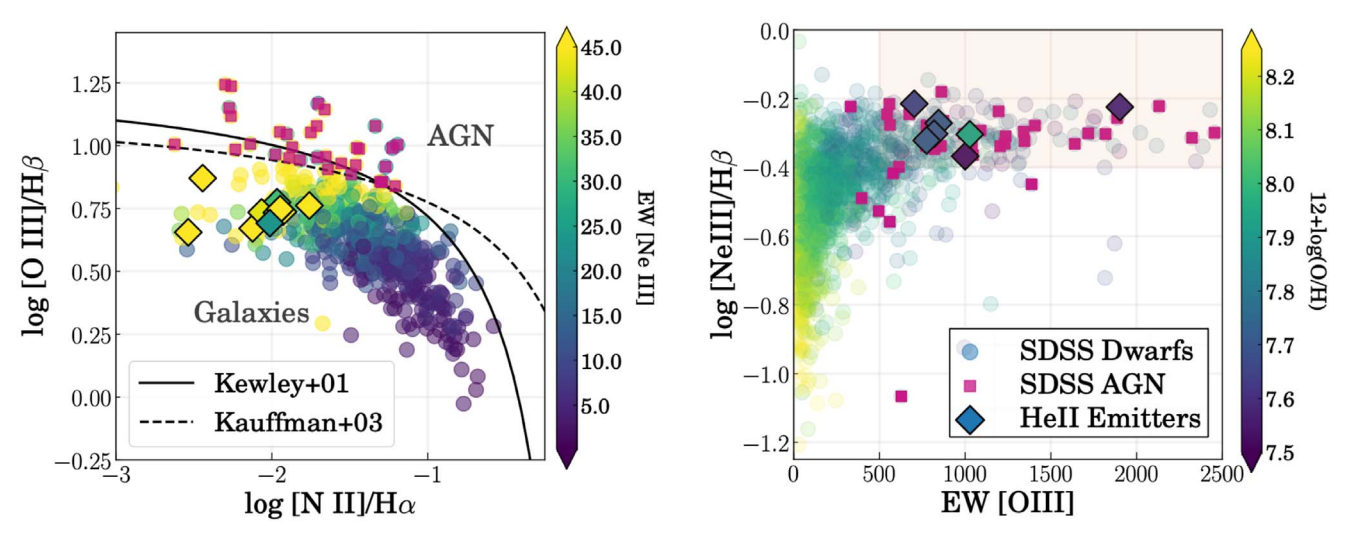


Figure 13. Emission-line ratios characterizing EELG He II emitters. Left: the $[O III]\lambda 5007/H\beta$ versus $[N II]\lambda 6584/H\alpha$ BPT diagram is plotted for a low-mass $(M_{\star} < 10^9 M_{\odot})$ subset of the SDSS DR14 (circles) and color-coded by the $[Ne III]\lambda 3868$ EW as a proxy for the strength of very high-ionization lines. The solid lines are the theoretical starburst limits from Kewley et al. (2001) and Kauffmann et al. (2003), designating outliers as AGN (magenta squares). In comparison, EELG He II emitters from Berg et al. (2016) and Berg et al. (2019b) occupy the upper left tail where excitation is high and metallicity is low. Right: For $[Ne III]\lambda 3868/H\beta$ versus the EW of $[O III]\lambda 5007$, the EELG He II emitters occupy the same upper right, extreme parameter space as AGN. These plots indicate that four-zone EELGs are likely produced by the combination of very high excitation and ionization with powerful emission relative to the stellar continuum.

for high-redshift galaxies, where only a few emission lines are typically observed. Therefore, we also quantified an ionization parameter typical of the *entire* four-zone nebulae of EELGs. To do so, we consider the ionization structure of our EELGs in Section 4.1, where the ionization fractions of oxygen suggested that the high-ionization zone is dominant in EELG nebulae, with very high-ionization zones that can be comparable to the low- to intermediate-ionization zones.

For J104457 and J141851, we found that the volume-averaged ionization parameters for the four-zone model (log $U_{\rm ave} = -1.70, -1.91$, respectively) are noticeably higher than those of the three-zone model (log $U_{\rm ave} = -1.77, -2.42$, respectively). This exercise has an important implication: ionization parameters in EELGs determined by the standard three-zone model misrepresent (underestimate) the steepness of the ionization structure and the volume-average ionization parameter. Given the known luminosity of observed EELGs, this may imply that the three-zone model underestimates the hardness of the underlying radiation field. Our forthcoming work (G. Olivier et al. 2021, in preparation) will further examine any implications the four-zone model has on the shape of the ionizing spectrum by simultaneously modeling the ionizing stellar population and suite of observed emission lines.

5.5. Recommendations for EELG Studies

Although our detailed abundance analyses are only for two EELGs, they provide an important benchmark with which to compare other EELGs, both near and far, and suggest diagnostic corrections. To determine when corrections are appropriate and most important, we examine how the properties of EELGs compare to a more general population of dwarf galaxies. In Figure 13 we plot extreme UV He II emitters (EW (He II $\lambda 1640$) > 1 Å) from Berg et al. (2019b) compared to dwarf galaxies ($M_{\star} < 10^9 M_{\odot}$) from the SDSS Data Release 14 (Blanton et al. 2017).

Figure 13 shows that He II EELGs occupy the limits of the high-ionization, low-metallicity parameter space in both the BPT (left panel) and the [Ne III] $\lambda 3868/H\beta$ vs

EW([O III] λ 5007) (right panel) diagnostic diagrams. These properties align with our expectations for EELGs and observed early universe galaxies: very high-ionization emission lines, such as He II, are produced in metal-poor galaxies with high star formation rates and hard radiation fields, as indicated by their large equivalent widths of high-ionization emission lines. These conditions, along with the observed *pure* very high-ionization emission lines, are indicative of the presence of a very high-ionization zone and require caution in interpreting their spectra.

By considering the parameter space occupied by nebular He II emitters, Figure 13 can be used to predict which galaxies are likely to have a very high-ionization zone. Specifically, good candidates can be identified with a combination of large [Ne III]/H β line ratios (>-0.4) indicating hard radiation fields and large [O III] EWs (>500 Å) indicating large specific star formation rates.

We have shown that EELGs have enhanced high-ionization zones and smaller low-ionization zones. In general, at higher ionization parameters, low-ionization lines, such as [O II] $\lambda 3727$, [N II] $\lambda\lambda 6548,84$, and [S II] $\lambda\lambda 6717,31$, have smaller fluxes and high-ionization lines, such as [Ne III] $\lambda 3868$ and [O III] $\lambda 5007$, have larger fluxes. This results in additional errors in strong-line metallicity measurements beyond their standard biases, and is especially important for high-redshift galaxies, where direct abundances are rarely accessible. Many of the strong-line calibrations involving low-ionization lines will *underestimate* both the calibrator and the true metallicity. These include:

- 1. N2 = $\log([N II] \lambda 6584/H\alpha)$,
- 2. $S2 = \log([S II] \lambda \lambda 6717,31/H\alpha),$
- 3. O32 = $\log([O III] \lambda 5007/[O II] \lambda 3727)$,
- 4. Ne3O2 = $\log([\text{Ne III}] \lambda 3868/[\text{O II}] \lambda 3727)$, and
- 5. O3N2 = $\log(([O III] \lambda 5007/H\beta)/([N II] \lambda 6584/H\alpha))$,

Other oxygen-based calibrations are double valued, such that R3 = log([O III] $\lambda 5007/H\beta$) will *overestimate* and R23 = log (([O II] $\lambda 3727+[O III] \lambda 5007)/H\beta$) will *underestimate* the true metallicity for 12+log(O/H) < 8.0 and >8.0, respectively. For

the Berg et al. (2019b) He II emitters, we measure $\log U_{\rm high}$ to be greater than $\log U_{\rm int}$ by 0.30 ± 0.15 dex.

We, therefore, recommend the following guidelines for very high-ionization galaxy candidates: (1) Ionization parameters inferred from [O III]/[O II] should be considered lower limits for very high-ionization galaxy candidates. (2) Strong-line oxygen abundances should be considered lower limits for most calibrations, while the R3 and R23 calibrators should be avoided all together.

6. Summary and Conclusions

We investigated the high-quality HST/COS UV and LBT/MODS optical spectra of two nearby, metal-poor *extreme emission-line galaxies* (EELGs), J104457 ($Z=0.058Z_{\odot}$) and J141851 ($Z=0.087Z_{\odot}$). These galaxies have very strong high-ionization nebular emission-line features, including He II λ 1640, C IV $\lambda\lambda$ 1548,1550, [Fe V] λ 4227, He II λ 4686, and [Ar IV] $\lambda\lambda$ 4711,4740 (see Figure 2 and 3), that liken them to reionization-era systems.

Typical stellar population models produce radiation fields that can only significantly ionize oxygen up to the O⁺² species. As a result, a fully ionized H II region is typically characterized by a three-zone model, with a low-ionization zone defined by N⁺ (14.5–20.6 eV), an intermediate-ionization zone defined by S^{+2} (23.3–34.8 eV), and a high-ionization zone defined by O^{+2} (35.1–54.9 eV). We showed this structure in Figure 4, where the outer edge of an H II region is defined by the lower H-ionizing edge (>13.6 eV) and extends inward to the upper limit of O⁺ (<54.9 eV). However, the ionization potentials of the very highionization lines observed here extend to energies higher than the upper limit of the standard three-zone ionization model and are indicative of very hard radiation fields. To better characterize the extreme, extended ionization parameter space of the nebular environments of EELGs, we define a new four-zone ionization model that includes the addition of a very high-ionization zone, characterized by the He^{+2} ion (>54.4 eV; see Figure 4).

Using the four-zone model, we measured the nebular properties and ionic abundances in each ionization zone of the two EELGs studied here and then used the results to reevaluate their average properties and structure. In general, we find that the addition of a very high-ionization zone has little to no effect on the integrated nebular abundances, but does change the interpretation of several physical properties of EELGs. Specifically, the main results of this work are:

1. Our four-zone determination of the nebular properties showed that temperature, density and ionization parameter peak in the very high-ionization zone of EELGs (Figure 8). To measure this, we adopted the commonly used temperature and density diagnostics for each zone of the standard three-zone model and added $T_e([Ne III]]$ $\lambda 3342/\lambda 3869$) (41.0 – 63.5 eV) and $n_e([Ar IV] \lambda 4711/$ $\lambda 4740$) (40.7 – 59.8 eV) diagnostics for the very highionization zone. Using these diagnostics, in the very highionization zones, we measured temperatures of T_e = $19,200 \pm 2300$ K and $23,600 \pm 3200$ K and densities of $n_e = 1550 \pm 1100$ cm⁻³ and 2100 ± 1300 cm⁻³ for J104457 and J141851, respectively. We also considered, for the first time, multiple ionization parameters to characterize different ionization zones, adopting: log $U_{low}([S III]/[S II])$, log $U_{int}([O III]/[O II])$, and log $U_{high}([Ar IV]/[Ar III]).$

- 2. Our four-zone determinations of total abundances in EELGs are consistent with the three-zone model when all relevant ions are observed. Specifically, we measured ionic abundances for all the relevant O ions (O⁰, O⁺, O⁺², and O⁺³) and Fe ions (Fe⁺, Fe⁺², Fe⁺³, and Fe⁺⁴) spanning the four-zone model. This result is also true for elements with ions observed from the dominant (high-) ionization zone, such as Ne and Ar. On the other hand, elements that only have observations of trace ions, such as N and S, likely have underestimated abundances.
- 3. We found a model-independent dichotomy in the abundance patterns, where the abundances for J104457 and J141851 fall into two groups: (1) α-element ratios that are consistent with measured oxygen abundances and a solar abundance pattern (O/H, Ar/H, Ne/H) and (2) relatively deficient element ratios (N/H, C/H, Fe/H).
- 4. The two abundance groups suggest that these EELGs are α /Fe-enriched by a factor of 3 or more, but this result alone cannot account for the properties of EELGs:
 - (a) We used photoionization models to show that α/Fe -enriched conditions in EELGs can produce high-ionization flux ratios that are augmented by up to 40% relative to solar- α/Fe EELGs (Figure 11. However, these models still fail to reproduce the large He II/H β ratios observed for EELGs by a factor of 5–10.
 - (b) While α/Fe enrichment may be responsible for the observed properties of typical $z \sim 2-3$ galaxies (e.g., Strom et al. 2017), we conclude there is an unsolved high-energy ionizing photon production problem, or HEIP³, in EELGs.
- 5. Regardless of the source, the very hard radiation fields in EELGs seem to produce higher central nebular temperatures, densities, and ionization parameters than previously thought. Using the measured O ion fractions as weights, we determined average ionization parameters of the four-zone model to be log *U* = −1.66 and −1.93 for J104457 and J141851, respectively, that are notably higher than the three-zone model average ionization parameters (log *U* = −1.77 and −2.42, respectively). Importantly, we showed in Figure 11 that these conditions support the model of a steeper central ionization structure than seen in more typical H II regions, which must be accounted for when determining properties of EELGs.

In summary, we found that the four-zone model is a more accurate representation of EELGs than the classical three-zone model, and the adoption of the four-zone model has a few important implications for the interpretation of these galaxies. Specifically, using the four-zone model reveals: (1) the presence of a central, compact, very high-ionization zone, (2) higher central gas-phase temperatures and densities and ionization parameters, (3) higher volume-averaged ionization parameters (log U) indicative of harder radiation fields, (4) increased abundances of N/H, S/H, and Fe/H, (5) negligible to small reductions in relative abundances of C/O, Ar/O and Ne/O, and (6) negligible changes in the overall O/H abundance, and (7) an unsolved it high-energy ionizing photon production problem (HEIP³). This work suggests that EELGs in both the local and distant universe have more extreme properties than previously thought. Therefore, future work with JWST and ELTs will likely require the four-zone model to diagnose accurate conditions within reionization-era galaxies.

D.A.B. is grateful for the support for this program, HST-GO-15465, that was provided by NASA through a grant from the Space Telescope Science Institute, which is operated by the Associations of Universities for Research in Astronomy, Incorporated, under NASA contract NAS5-26555. D.K.E. is supported by the US National Science Foundation (NSF) through the Astronomy & Astrophysics grant AST-1909198. We are also grateful to the referee for thoughtful feedback that greatly improved the clarity of this paper.

This work also uses observations obtained with the Large Binocular Telescope (LBT). The LBT is an international collaboration among institutions in the United States, Italy, and Germany. LBT Corporation partners are: The University of Arizona on behalf of the Arizona Board of Regents; Istituto Nazionale di Astrofisica, Italy; LBT Beteiligungsgesellschaft, Germany, representing the Max-Planck Society, The Leibniz Institute for Astrophysics Potsdam, and Heidelberg University; The Ohio State University, University of Notre Dame, University of Minnesota, and University of Virginia.

This paper made use of the modsIDL spectral data reduction reduction pipeline developed in part with funds provided by NSF grant AST-1108693 and a generous gift from OSU Astronomy alumnus David G. Price through the Price Fellowship in Astronomical Instrumentation. Photoionization models were run with CLOUDY, which is currently supported by grants from NSF (AST 1816537 and AST 1910687 National Aeronautics and Space Administration 19-ATP19-0188) and Space Telescope Science Institute (HST-AR-15018). These models also made use of v2.1 of the Binary Population and Spectral Synthesis (BPASS) models, as last described in Eldridge et al. (2017).

Facilities: LBT (MODS), HST (COS)

Software: CLOUDY 17.00 (Ferland et al. 2013) DUSTMAPS (Green 2018), modsIDL pipeline (?), STARLIGHT (Fernandes et al. 2005), XIDL (http://www.ucolick.org/xavier/IDL/), PYNEB (Luridiana et al. 2012, 2015)

Appendix Structure of Ionic Species

To better understand the structure of EELGs, we explore the ionization structure of different elements using the photoionization model grid described in Section 3.1.1. In Figure 14 we plot how the ionization fractions of different species change as a function of relative H II region radius from the central ionizing source and for different input ionization parameters. We show plots for three different ionization parameters, with EELGs represented by the log U=-1 model in the top row, compared to the log U=-2 model in the middle row, and the log U=-3 model that is characteristic of average H II regions in the bottom row. Figure 14 is further separated into columns categorized by the ionization zones of the four-zone model.

As a whole, the $\log U = -3$ model in Figure 14 shows some ions contributing significantly from each of the low-, intermediate- and high-ionization zones, where the high-ionization ions dominate in the inner 50%-75% of the nebula and the low-ionization ions dominate in the complimentary outer regions. In this model, no very high-ionization ion makes a significant contribution, and therefore confirms the three-zone model as the appropriate model for typical H II regions. In contrast, the $\log U = -1$ model in Figure 14 shows that the high- and very high-ionization ions dominate the ionization fractions over the majority of the nebula. Very little contribution is seen from low- or intermediate-ionization ions on average, as their small contributions only take effect at the very outer edges of the nebula. This structure highlights the importance of using the four-zone model to interpret EELGs.

When comparing the different log U models for the very high-ionization zone (last column), we not only see that ionization fractions of these elements significantly increase with higher log U, but also see their shapes drastically change. For example, in the log U=-3 model, the He^{+2} ion (solid yellow line) peaks in the center of the nebula at a fraction of $\sim 1\%$, and then somewhat gradually falls off with radius, reaching $\sim 0.0001\%$ at the outer edge of the nebula. In contrast, in the log U=-1 model, the He^{+2} ion reaches a much higher peak of $\sim 50\%$, but quickly falls off to the same $\sim 0.0001\%$ at only $\sim 5\%$ of the relative radius of the nebula. This supports the idea of a central, very compact very high-ionization zone, where the ionization structure is much more steeply declining than that of a typical nebula.

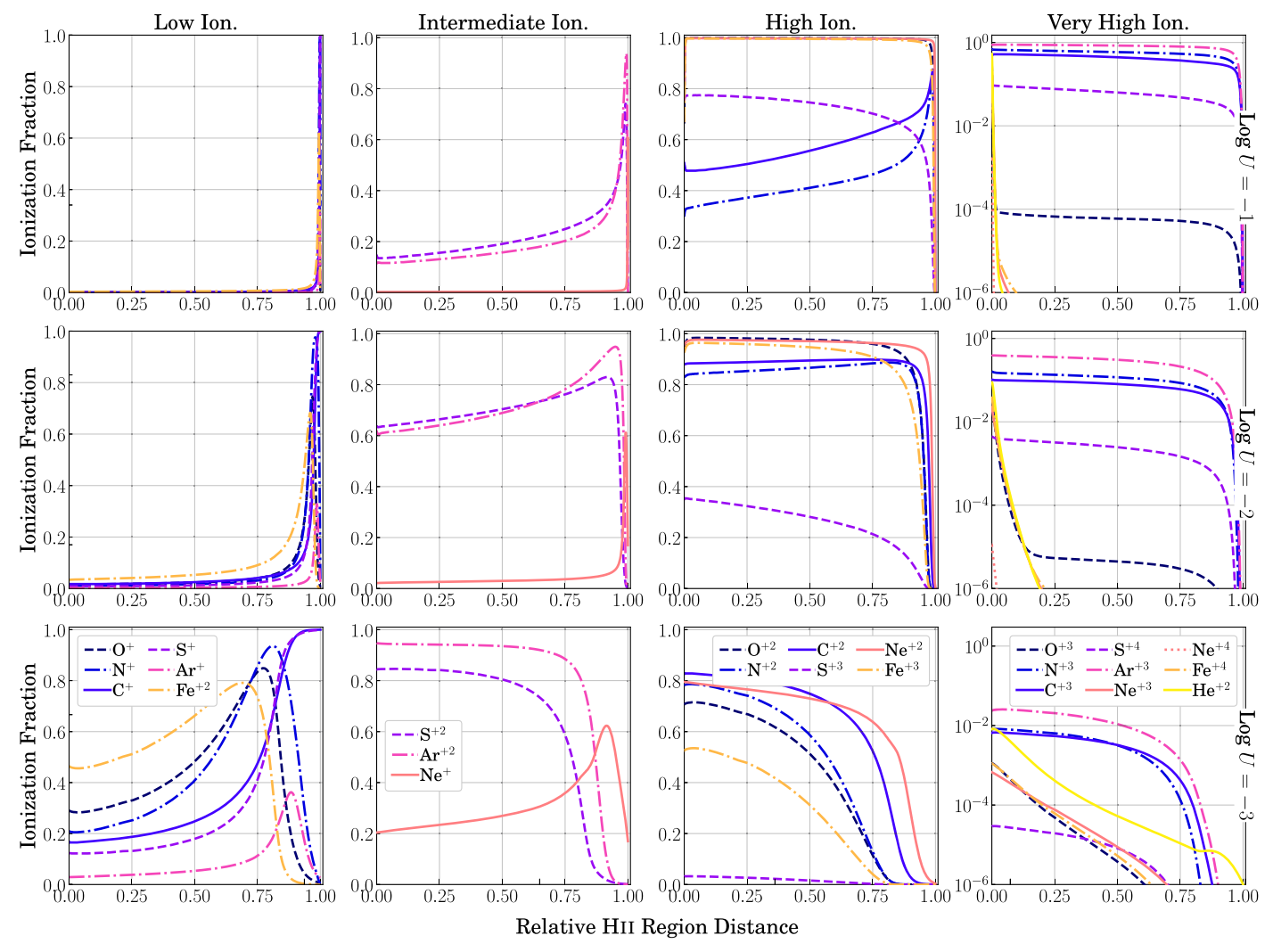


Figure 14. Photoionization models showing how ionization fractions of different species change as a function of relative H II region radius.

ORCID iDs

Danielle A. Berg https://orcid.org/0000-0002-4153-053X John Chisholm https://orcid.org/0000-0002-0302-2577 Dawn K. Erb https://orcid.org/0000-0001-9714-2758 Evan D. Skillman https://orcid.org/0000-0003-0605-8732 Richard W. Pogge https://orcid.org/0000-0003-1435-3053 Grace M. Olivier https://orcid.org/0000-0002-4606-4240

References

Atek, H., Richard, J., Kneib, J.-P., & Schaerer, D. 2018, MNRAS, 479, 5184 Atek, H., Siana, B., Scarlata, C., et al. 2011, ApJ, 743, 121 Berg, D. A., Chisholm, J., Erb, D. K., et al. 2019a, ApJL, 878, L3 Berg, D. A., Erb, D. K., Auger, M. W., Pettini, M., & Brammer, G. B. 2018, I, 859, 164 Berg, D. A., Erb, D. K., Henry, R. B. C., Skillman, E. D., & McQuinn, K. B. W. 2019b, ApJ, 874, 93 Berg, D. A., Pogge, R. W., Skillman, E. D., et al. 2020, ApJ, 893, 96 Berg, D. A., Skillman, E. D., Croxall, K., et al. 2015, ApJ, 806, 16 Berg, D. A., Skillman, E. D., Henry, R. B. C., Erb, D. K., & Carigi, L. 2016, ApJ, 827, 126 Berg, D. A., Skillman, E. D., & Marble, A. 2011, ApJ, 738, 2 Berg, D. A., Skillman, E. D., Marble, A., et al. 2012, ApJ, 754, 98 Blanton, M. R., Bershady, M. A., Abolfathi, B., et al. 2017, AJ, 154, 28 Bouwens, R. J., Illingworth, G. D., Oesch, P. A., et al. 2015, ApJ, 803, 34 Bruzual, G., & Charlot, S. 2003, MNRAS, 344, 1000 Cardelli, J. A., Clayton, G. C., & Mathis, J. S. 1989, ApJ, 345, 245

Chevallard, J., Charlot, S., Senchyna, P., et al. 2018, MNRAS, 479, 3264 Chisholm, J., Tremonti, C., & Leitherer, C. 2018, MNRAS, 481, 1690 Christensen, L., Laursen, P., Richard, J., et al. 2012, MNRAS, 427, 1973 Costas, V. B. M., & Edmunds, M. G. 1993, MNRAS, 265, 199 Dale, D. A., Cohen, S. A., Johnson, L. C., et al. 2009, ApJ, 703, 517 De Barros, S., Oesch, P. A., Labbé, I., et al. 2019, MNRAS, 489, 2355 Dopita, M. A., Kewley, L. J., Heisler, C. A., & Sutherland, R. S. 2000, ApJ, 542, 224 Eldridge, J. J., & Stanway, E. R. 2016, MNRAS, 462, 3302 Eldridge, J. J., Stanway, E. R., Xiao, L., et al. 2017, PASA, 34, e058 Endsley, R., Stark, D. P., Chevallard, J., & Charlot, S. 2021, MNRAS, 500, 5229 Esteban, C., Bresolin, F., García-Rojas, J., & Toribio San Cipriano, L. 2020, MNRAS, 491, 2137 Esteban, C., Bresolin, F., Peimbert, M., et al. 2009, ApJ, 700, 654 Ferland, G. J., Porter, R. L., van Hoof, P. A. M., et al. 2013, RMxAA, 49, 137 Fernandes, I. F., Gruenwald, R., & Viegas, S. M. 2005, MNRAS, 364, 674 Filippenko, A. V. 1982, PASP, 94, 715 Finkelstein, S. L., Ryan, R. E., Jr., Papovich, C., et al. 2015, ApJ, 810, 71 Garnett, D. R., Dufour, R. J., Peimbert, M., et al. 1995, ApJL, 449, L77 Green, G. 2018, JOSS, 3, 695 Green, G. M., Schlafly, E. F., Finkbeiner, D. P., et al. 2015, ApJ, 810, 25 Grevesse, N., Asplund, M., Sauval, A. J., & Scott, P. 2010, Ap&SS, 328, 179 Guseva, N. G., Izotov, Y. I., Papaderos, P., et al. 2001, A&A, 378, 756 Henry, R. B. C., Edmunds, M. G., & Köppen, J. 2000, ApJ, 541, 660 Hill, J. M., Green, R. F., Ashby, D. S., et al. 2010, Proc. SPIE, 7733, 77330C Hutchison, T. A., Papovich, C., Finkelstein, S. L., et al. 2019, ApJ, 879, 70 Izotov, Y. I., Guseva, N. G., Fricke, K. J., & Papaderos, P. 2009, A&A, 503, 61 Izotov, Y. I., Stasińska, G., Meynet, G., Guseva, N. G., & Thuan, T. X. 2006, A&A, 448, 955

```
Izotov, Y. I., & Thuan, T. X. 2007, ApJ, 665, 1115
Janowiecki, S., Salzer, J. J., van Zee, L., Rosenberg, J. L., & Skillman, E. 2017,
    ApJ, 836, 128
Kauffmann, G., Heckman, T. M., Tremonti, C., et al. 2003, MNRAS,
  346, 1055
Kehrig, C., Vílchez, J. M., Guerrero, M. A., et al. 2018, MNRAS, 480, 1081
Kehrig, C., Vílchez, J. M., Pérez-Montero, E., et al. 2015, ApJL, 801, L28
Kewley, L. J., Dopita, M. A., Sutherland, R. S., Heisler, C. A., & Trevena, J.
   2001, ApJ, 556, 121
Kobayashi, C., Karakas, A. I., & Lugaro, M. 2020, ApJ, 900, 179
Labbé, I., Oesch, P. A., Bouwens, R. J., et al. 2013, ApJL, 777, L19
Laporte, N., Nakajima, K., Ellis, R. S., et al. 2017, ApJ, 851, 40
Levesque, E. M., & Richardson, M. L. A. 2014, ApJ, 780, 100
Livermore, R. C., Finkelstein, S. L., & Lotz, J. M. 2017, ApJ, 835, 113
Luridiana, V., Morisset, C., & Shaw, R. A. 2012, in IAU Symp. 283, Planetary
   Nebulae: An Eye to the Future (Cambridge: Cambridge Univ. Press), 422
Luridiana, V., Morisset, C., & Shaw, R. A. 2015, A&A, 573, A42
Madau, P., & Haardt, F. 2015, ApJL, 813, L8
Mainali, R., Kollmeier, J. A., Stark, D. P., et al. 2017, ApJL, 836, L14
Mainali, R., Zitrin, A., Stark, D. P., et al. 2018, MNRAS, 479, 1180
Maseda, M. V., van der Wel, A., da Cunha, E., et al. 2013, ApJL, 778, L22
Maseda, M. V., van der Wel, A., Rix, H.-W., et al. 2014, ApJ, 791, 17
McGreer, I. D., Clément, B., Mainali, R., et al. 2018, MNRAS, 479, 435
Moustakas, J., Kennicutt, R. C. J., Tremonti, C. A., et al. 2010, ApJS, 190, 233
Nava, A., Casebeer, D., Henry, R. B. C., & Jevremovic, D. 2006, ApJ,
   645, 1076
Oesch, P. A., Montes, M., Reddy, N., et al. 2018, ApJS, 237, 12
Oke, J. B. 1990, AJ, 99, 1621
Papaderos, P., Guseva, N. G., Izotov, Y. I., & Fricke, K. J. 2008, A&A,
   491, 113
Peeples, M. S., & Shankar, F. 2011, MNRAS, 417, 2962
Peimbert, M., & Costero, R. 1969, BOTT, 5, 3
Pilyugin, L. S., Mattsson, L., Vílchez, J. M., & Cedrés, B. 2009, MNRAS,
   398, 485
Pogge, R. W., Atwood, B., Brewer, D. F., et al. 2010, Proc. SPIE, 7735,
   77350A
Pustilnik, S., Kniazev, A., Pramskij, A., et al. 2004, A&A, 419, 469
```

```
Reddy, N. A., Steidel, C. C., Pettini, M., Bogosavljević, M., & Shapley, A. E.
  2016, ApJ, 828, 108
Reyes, R., Mandelbaum, R., Gunn, J. E., Pizagno, J., & Lackner, C. N. 2011,
         AS, 417, 2347
Rigby, J. R., Bayliss, M. B., Gladders, M. D., et al. 2015, ApJL, 814, L6
Robertson, B. E., Ellis, R. S., Furlanetto, S. R., & Dunlop, J. S. 2015, ApJL,
  802, L19
Rodríguez, M. 1999, A&A, 348, 222
Rodríguez, M. 2003, ApJ, 590, 296
Rodríguez, M., & Rubin, R. H. 2005, ApJ, 626, 900
Schmidt, K. B., Huang, K.-H., Treu, T., et al. 2017, ApJ, 839, 17
Senchyna, P., Stark, D. P., Chevallard, J., et al. 2019, MNRAS, 488, 3492
Senchyna, P., Stark, D. P., Vidal-García, A., et al. 2017, MNRAS, 472, 2608
Shapley, A. E., Sanders, R. L., Shao, P., et al. 2019, ApJL, 881, L35
Smit, R., Bouwens, R. J., Franx, M., et al. 2015, ApJ, 801, 122
Smit, R., Swinbank, A. M., Massey, R., et al. 2017, MNRAS, 467, 3306
Sobral, D., Matthee, J., Darvish, B., et al. 2015, ApJ, 808, 139
Stanway, E. R., & Eldridge, J. J. 2019, A&A, 621, A105
Stanway, E. R., Eldridge, J. J., & Becker, G. D. 2016, MNRAS, 456, 485
Stark, D. P. 2016, ARA&A, 54, 761
Stark, D. P., Ellis, R. S., Charlot, S., et al. 2017, MNRAS, 464, 469
Stark, D. P., Richard, J., Charlot, S., et al. 2015, MNRAS, 450, 1846
Stark, D. P., Richard, J., Siana, B., et al. 2014, MNRAS, 445, 3200
Steidel, C. C., Bogosavljević, M., Shapley, A. E., et al. 2018, ApJ, 869, 123
Strom, A. L., Steidel, C. C., Rudie, G. C., et al. 2017, ApJ, 836, 164
Tang, M., Stark, D., Chevallard, J., et al. 2021, MNRAS, 501, 3238
Tang, M., Stark, D. P., Chevallard, J., & Charlot, S. 2019, MNRAS, 489, 2572
Thuan, T. X., Izotov, Y. I., & Lipovetsky, V. A. 1995, ApJ, 445, 108
Topping, M. W., Shapley, A. E., Reddy, N. A., et al. 2020, MNRAS, 495, 4430
van der Wel, A., Straughn, A. N., Rix, H. W., et al. 2011, ApJ, 742, 111
van Zee, L., & Haynes, M. 2006, ApJ, 636, 214
Vanzella, E., Balestra, I., Gronke, M., et al. 2017, MNRAS, 465, 3803
Vanzella, E., De Barros, S., Cupani, G., et al. 2016, ApJL, 821, L27
Weinberg, D. H., Andrews, B. H., & Freudenburg, J. 2017, ApJ, 837, 183
Wise, J. H., Demchenko, V. G., Halicek, M. T., et al. 2014, MNRAS,
  442, 2560
```